Master of Science Thesis

Numerical Study of Turbulence Induced Vibrations Using Synthetic Fluctuation Field Modeling in Nuclear Reactor Applications

Saurabh Sharma

March 20, 2018

Aerodynamics

Faculty of Aerospace Engineering

TU Delft

Delft University of Technology

Numerical Study of Turbulence Induced Vibrations Using Synthetic Fluctuation Field Modeling in Nuclear Reactor Applications

Master of Science Thesis

For obtaining the degree of Master of Science in Aerospace Engineering
at Delft University of Technology

Saurabh Sharma

March 20, 2018

Faculty of Aerospace Engineering · Delft University of Technology

Delft University of Technology

DELFT UNIVERSITY OF TECHNOLOGY
DEPARTMENT OF AERODYNAMICS

The undersigned hereby certify that they have read and recommend to the Faculty of Aerospace Engineering for acceptance the thesis entitled **"Numerical Study of Turbulence Induced Vibrations Using Synthetic Fluctuation Field Modeling in Nuclear Reactor Applications"** by **Saurabh Sharma** in fulfillment of the requirements for the degree of **Master of Science**.

Dated: March 20, 2018

Supervisors:

Dr. A. (Afaque) Shams

Dr. Ir. A.H. (Alexander) van Zuijlen

Dr.ir. M.I. (Marc) Gerritsma

Dr.ir. M.J.B.M. (Mathieu) Pourquie

Preface

This document is the final report for the Master of Science thesis project. I would like to take this opportunity here to thank the people who guided and supported me during the course of this project. Firstly I would like to thank my supervisors Dr. Afaque Shams and Dr. Ir. Alexander van Zuijlen for their constant guidance throughout the entirety of this project. Their supervision and suggestions are highly appreciated. I would also like to thank Shravan Kottapalli and Dante De Santis for helping me get acquainted with OpenFOAM and answering my endless queries on the same. I would also like to thank the Nuclear Research and Consultancy Group (NRG) for giving me the opportunity to complete my thesis at their institute and letting me use their computational resources. I also appreciate the support of all my colleagues at NRG who made my stay in Alkmaar a lot more fun.

I would also like to thank my friends at TU Delft who made this period of study less stressful and way more enjoyable. Lastly I would like to thank my parents for always believing in me and their unwavering support for my education.

Delft, March 2017

Abstract

The nuclear technology is changing at a rapid pace driven by the quest for more powerful and safer nuclear power plants, as a consequence several structural components in a reactor are becoming larger and slender while working fluids have higher densities and velocities. These changes can often alter the dynamics of the interaction between the coolant and the structural components and cause Flow Induced Vibrations (FIV) to become more prominent. As analytical methods are often insufficient to predict FIV in complex geometries, numerical approaches are commonly used to predict such phenomena.

Of all the possible modes of excitation in a nuclear reactor, simulating Turbulence Induced Vibrations (TIV) is a particularly challenging problem due to the wide range of scales involves, and is the main focus of this thesis work. Ideally high fidelity fluid solvers using DNS or LES can be used to resolve all the scales involved, but such methods are computationally expensive for complex domains with high Reynolds numbers. In this work, an alternative method to using high fidelity solvers is presented, which involves synthetically modeling the turbulent fluctuations using the known turbulence parameters from U-RANS simulations. These fluctuation fields are then superimposed on top of the average fields and act as the required excitement at the fluid structure interface. The numerical framework in which this method is implemented is first validated with known benchmark cases and it is found that the solver produces accurate results which are in good agreement with the reference data. The capabilities of the synthetic fluctuation modeling in simulating TIV are then assessed by performing simulations of a configuration adopted from an experimental set-up. It is observed that this model is able to reproduce the dynamics of the vibrations observed in the experiments while classical U-RANS model fails to predict physical oscillations.

Table of Contents

Preface vi

Abstract viii

List of Figures xiii

List of Tables xvii

1 Introduction 1

1.1 Nuclear Reactors . . . 2

1.2 Flow Induced Vibrations . . . 3

1.3 Research Objective . . . 5

1.4 Thesis Outline . . . 6

2 Numerical Methodology 7

2.1 Frames of Reference . . . 7

2.2 Fluid Dynamics . . . 8

2.3 Structural Dynamics . . . 10

2.4 Finite Volume Discretization . . . 10

2.4.1 Solution Domain Discretization . . . 10

2.4.2 Equation Discretization . . . 11

2.4.2.1 Convection Term . . . 12
2.4.2.2 Diffusion Term . . . 12
2.4.2.3 Source Term . . . 13
2.4.2.4 Temporal Discretization . . . 13
2.4.3 System of Algebraic Equations . . . 13
2.5 Coupling of Fluid and Structural domains . . . 14
2.5.1 Coupling Algorithm . . . 14
2.6 Summary . . . 18

3 Synthetic Modeling of Pressure Fluctuations 19

3.1 RANS Methods . . . 20
3.2 Modeling the Synthetic Fluctuation Fields . . . 22
3.2.1 Energy Cascade . . . 23
3.2.2 Velocity Fluctuation Modeling as Fourier Series . . . 25
3.2.3 Calculating the pressure fluctuation field and traction at the fluid-surface interface . . . 28
3.3 Numerical Code . . . 29
3.4 Influence of Using Separate Time Marching Schemes for Fluid and Solid Domain 29
3.5 Summary . . . 29

4 Validation of preCICE Coupling 31

4.1 Numerical Benchmark . . . 31
4.1.1 Domain Description . . . 32
4.1.2 Boundary Conditions . . . 32
4.1.3 Physical Properties and Simulation Setup . . . 33
4.1.4 Results and Discussions . . . 34
4.1.4.1 Hron and Turek CSM3 . . . 34
4.1.4.2 Hron and Turek CFD3 . . . 35
4.1.4.3 Hron and Turek FSI3 . . . 36

4.2 Experimental Benchmark . . . 38
4.2.1 Experimental Setup . . . 38
4.2.2 Computational Domain . . . 39
4.2.3 Structure Only Simulation . . . 40
4.2.4 Coupled Fluid Structure Interaction . . . 41
4.2.4.1 Fluid Grid Independence . . . 43
4.2.4.2 Results and Discussion . . . 44
4.3 Summary . . . 45

5 Validation of Synthetic Turbulent Fluctuations for TIV **47**
5.1 **Steel flap fixed on both ends** . . . 47
5.2 3-D Cantilever Rod in Axial Water Flow . . . 49
5.2.1 Experiment Description . . . 49
5.2.2 Structure Only Simulation . . . 49
5.2.3 Coupled FSI Simulation . . . 51
5.2.3.1 Results and Discussions . . . 53
5.3 Summary . . . 55

6 Conclusions **57**

A Influence of Time Marching **59**
A.1 Model Problem . . . 59
A.1.1 Equations governing the fluid and structure domain . . . 60
A.2 Time Integration . . . 63
A.2.1 Monolithic Approach . . . 63
A.2.2 Partitioned Approach . . . 63
A.3 Numerical Results . . . 64

Bibliography **69**

List of Figures

1.1 Schematic: Pressurised water reactor 2

1.2 Cross section of reactor vessel (PWR) 3

1.3 Vibration excitation mechanisms 4

2.1 Computational cell (control volume) in Finite Volume Methodology 11

2.2 Schematic of the interface of a fluid and structural domain 15

3.1 Ensemble average of 3 samples of velocity measured at a point in turbulent flow 21

3.2 Energy spectrum for a turbulent flow field 24

3.3 k_n and σ_n for n-th Fourier Mode 26

4.1 Computational domain showing the fluid and the structural domain (Gatzhammer, 2014) 32

4.2 Mesh-coarse 33

4.3 Mesh-fine1 33

4.4 Mesh-fine2 34

4.5 y-displacement of point-A (CSM3) 35

4.6 Close-up of the gap between cylindical and beam section of the structure (Sheldon, 2012) 35

4.7 Velocity contours at t = 5s [m/s] (CFD3) 36

4.8 Pressure contours at t = 5s [Pa] (CFD3) 36

4.9 Lift force on the cylinder + beam (CFD3) 36

4.10 Drag force on the cylinder + beam (CFD3) 36

4.11 Velocity contours at t = 10s (in m/s) 37

4.12 y-displacement of point A (FSI3) 37

4.13 Boundary conditions of the steel beam at different locations 39

4.14 Schematic of steps involved in displacing the beam 39

4.15 Dimensions of the Vattenfall computational domain 40

4.16 Displacement history for simulations with varying number of axial elements (BE and CN represent Backward Euler Crank-Nicolson time integration schemes respectively) 41

4.17 Displacement history for simulations with 640 and 1280 axial elements 41

4.18 Fluid (black) and structure (blue) mesh used for the FSI simulation 42

4.19 Displacement history of the center of the beam with varying grades on fluid mesh 43

4.20 Displacement history of the center of the beam for simulation with water flow of 1m/s 44

4.21 Displacement history of the center of the beam during coupled fluid and structure simulation 45

5.1 Mesh and domain of the Steel Flap in Turbulent Water test case. The length of the fluid domain (in blue) $L = 3.15\ m$, height of the fluid domain $H = 400\ mm$, length of the flap (in black) $l = 2\ m$ and the width of the flap $h = 20\ mm$. . . . 48

5.2 Comparison of the structural displacement of the beam center with and without the synthetic turbulent fluctuations 48

5.3 Schematic of the test facility 50

5.4 Variations of the rod free end 50

5.5 Fast Fourier Transform of the displacement histories for different grades of structural mesh (red squares show the dominant frequency) 51

5.6 Different view of the computational mesh uses for the the fluid (black) and structure domain (blue). (a) Isometric view (b) Fluid Outlet (c) Fluid Inlet 52

5.7 Velocity, pressure and turbulent kinetic energy field for a cross-section of the computational domain (3-D Cantilever Rod in Axial Water Flow) 53

5.8 Zoomed view of the velocity, pressure and turbulent kinetic energy field for a cross-section of the computational domain (3-D Cantilever Rod in Axial Water Flow) . 53

5.9 Displacement history of rod free end for U-RANS simulation without synthetic fluctuation modeling 54

5.10 Displacement history of rod free end for U-RANS simulation with synthetic fluctuation modeling 55

A.1 1-D piston problem 59

A.2 Structural displacement and velocity for the 1-D piston problem 65

A.3 Structural velocity error 66

A.4 Fluid density perturbation field error 66

A.5 Structural displacement error 66

A.6 Partitioning error 67

A.7 Eigenvalues of matrix A corresponding to Eq. (A.13) with reference to the stability regions of BDF1, 2 and 3 68

A.8 Closeup of the eigenvalues (showing some are within the instability region of BDF3) 68

List of Tables

4.1 Physical parameters for test cases performed 33

4.2 Mean and amplitude of the y-displacement of point A for FSI3 38

4.3 Frequency of oscillation for each of the simulated cases (BE and CN represent Backward Euler and Crank-Nicolson time integration schemes respectively) . . . 41

4.4 Boundary conditions for the flow variables in OpenFOAM 42

4.5 Settings for the solver 43

5.1 Comparison of r.m.s values of the displacement of the flap 49

5.2 Oscillation frequency for different grades of structural mesh 51

5.3 Material properties used in 3-D cantilever rod case 52

5.4 Comparison of the maximum displacement observed in the simulations with the experimental data 54

A.1 Time integration methods analyzed for the fluid and structure sub-domains . . . 64

Chapter 1

Introduction

Out of all the available means of energy production, nuclear reactors possess the highest energy density. This means that per unit mass of the fuel used, nuclear reactors produce the highest amount of usable energy. With the ever increasing demand for energy globally, the steady rise in global average temperatures and thus the need to reduce humanity's dependence on fossil fuels, alternate sources of energy are required. As fully sustainable solutions are still developing and are dependent on geographical locations, nuclear energy can be used as a viable source for immediate energy requirements. The high energy density which makes nuclear energy lucrative also leads to the safety being of critical importance as any accident can lead to radioactive contamination. In a typical nuclear reactor the heat generated in the nuclear core from the fuel rods is carried away by the coolants to generate high pressure steam from water which in turn is then used to run turbines to generate electricity. The fluid used to absorb the heat from the fuel rods and carry it to the turbines is called the coolant fluid. The flow of this fluid around various flexible components of the reactor (e.g. the heat exchangers and the fuel rods) can lead to Flow Induced Vibrations (FIV) . These flow induced vibrations play a critical role in nuclear safety as they can lead to fatigue wear, fretting wear, stress corrosion cracking and other possible failure modes (Luk, 1993; Paı et al., 2006). Reports of reactor damage due to flow induced vibrations in heat exchanger tubes started appearing in 1950s (Weaver et al., 2000). The research in the field of nuclear reactors is being driven by the demand for increasing the power density of the nuclear plants. This often leads to increase in the coolant flow rate, a change of coolant fluid or modifying the materials and dimensions of structural components. These changes can often alter the dynamics of the interaction between the coolant and the structural components and cause flow induced vibrations to become more prominent (Weaver et al., 2000). Therefore an accurate prediction of flow induced vibrations to asses the risk early in the design phase of a reactor is an important area of research.

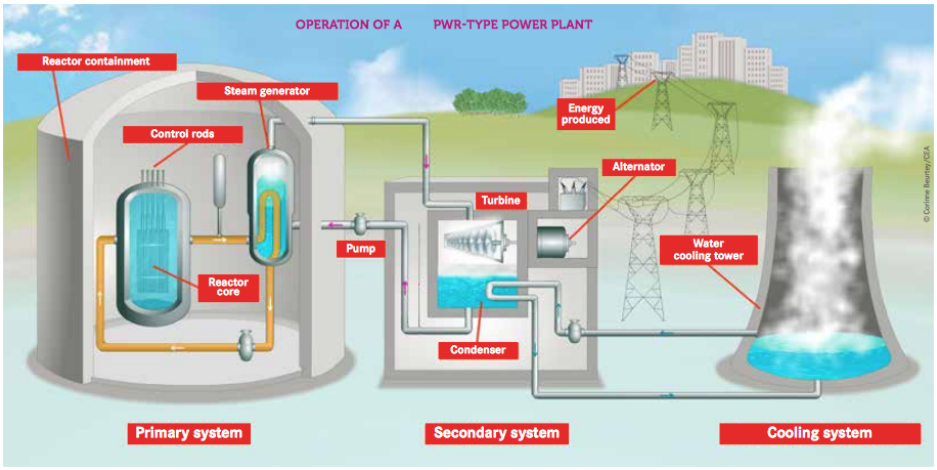

Figure 1.1: Schematic: Pressurised water reactor

1.1 Nuclear Reactors

Since this report is focused on the fluid structure interaction problems in a nuclear reactor, a brief overview of their functioning is provided. A general schematic of a nuclear reactor is shown in Fig. 1.1. Essentially a nuclear reactor is designed to recover and transport the heat generated by fission reactions in the nuclear core up to a turbine to generate electricity. The generated heat is first absorbed used a cooling fluid around the reactor core, which is then used to generate steam, finally the steam is used to run the turbines. The parts of the reactor where the fluid structure interaction being studied occurs is the nuclear reactor vessel. This is a pressure vessel containing the reactor core and the coolant fluid and is explained in more detail later.

Nuclear reactors are usually classified by their generation. The first generation reactors were developed in 1950s and 60s. These included the prototypes and some of the first full scale industrial reactors meant to serve as proof for their economic viability. The second generation reactors were commissioned from early 1970s and were designed with the goal of increased competitiveness during the period of oil crisis. The third generation reactors prioritized safety and security from internal and external hazards. This was a response to major accidents like Chernobyl and Three Mile Island. Most of the nuclear reactors currently in use or commissioned for construction are third generation reactors. Fourth generation nuclear reactors are currently in research phase with the main objectives being increased power density, improved efficiency and sustainability. Another common way to classify nuclear reactors is on the basis of the coolant being used e.g. Pressurized Water Reactor (the most common reactor used at present), Boiling Water Reactors (BWR), Gas Cooled reactor (GCR), Fast Breeder Reactors (FBR), Pressurized Heavy Water Reactor (PHWR).

Fig. 1.2 below shows the cross section of the reactor pressure vessel of a pressurized water reactor (PWR). In the PWR, water at high pressure and temperature absorbs heat from the

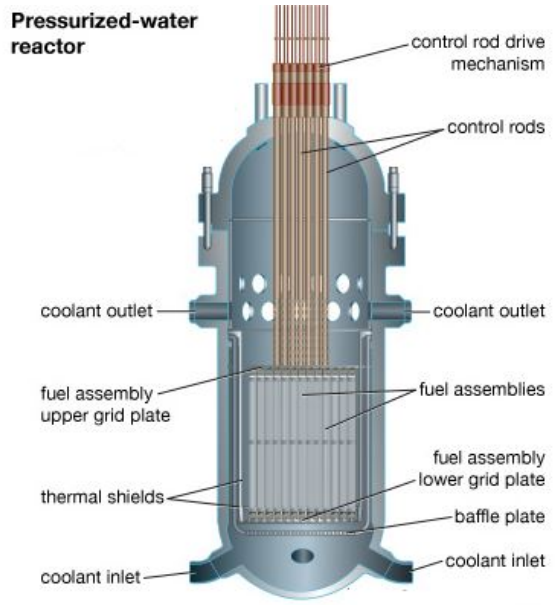

Figure 1.2: Cross section of reactor vessel (PWR)

fuel rods and transports it to a steam generator. This is known as the primary loop. The heat from this loop is then transferred to water at a lower pressure i.e. the secondary loop. The water in the secondary loop absorbs the heat from the primary loop to obtain saturated and superheated steam. This steam is then directed to a turbine to generate electricity. The coolant flowing around the fuel rods is generally in the turbulent regime, especially at higher mass flow rates. The flow conditions inside the reactor vessel can lead to several Fluid Structure Interaction (FSI) phenomena such as vortex shedding, fluid elastic instability, etc, which are discussed in the next section. Such interactions can lead to vibrations that may ultimately lead to catastrophic failure of the structural components. As is obvious, safety is of paramount importance in nuclear reactors and hence it is important to be able to predict the dynamic behavior of such systems using numerical tools.

1.2 Flow Induced Vibrations

Flow Induced Vibrations is a broad term used to describe any phenomenon that is associated with the response of a structure immersed in any fluid. Different parts of the nuclear reactor can vibrate due to to entirely different excitation mechanisms, e.g. the flow around fuel rods is axial whereas the steam generator tubes have both axial and cross flow. The type of flow along the fuel rods could be either gas, liquid or even a mixture of both. Such flow conditions decide the nature of interaction between the structure and the fluid. Different vibration excitation mechanisms which can be present in nuclear reactors are mentioned below:

Flow situation	Fluidelastic instability	Periodic shedding	Turbulence excitation	Acoustic resonance
Axial flow				
Internal				
Liquid	*	—	**	***
Gas	*	—	*	***
Two-phase	*	—	**	*
External				
Liquid	**	—	**	***
Gas	*	—	*	***
Two-phase	*	—	**	*
Cross flow				
Single cylinders				
Liquid	—	***	**	*
Gas	—	**	*	*
Two-Phase	—	*	**	—
Tube Bundle				
Liquid	***	**	**	*
Gas	***	*	*	***
Two-phase	***	*	**	—

***Most important.
**Should be considered.
*Less likely.
—, Does not apply.

Steam generator
Fuel rods
Steam generator and fuel rods

Figure 1.3: Vibration excitation mechanisms Luk (1993)

1. **Fluid Elastic Instability**: The flow field around the fuel rod displaces the rod from its initial position. This displacement further changes the flow field and hence the fluid forces on the rod. The damping forces in the structure try to restore the fuel rod to its initial position resulting in a competition between energy input by fluid forces and energy dissipation by damping. Vibrations occurs when the fluid dynamic forces are greater than the energy being dissipated by the structural damping.

2. **Periodic vortex shedding**: Vortices are periodically shed downstream of structures in cross flow. This induces periodic pressure variations on the structure surface that may lead to vibrations in the transverse or the flow direction. If this periodicity coincides with the natural frequency of the the structure, resonance may occur

3. **Acoustic resonance**: This excitation occurs when the vortex shedding frequency coincides with the natural frequency of the acoustic cavity formed by the structures surrounding the tube bundles. The other necessary condition is that the energy supplied by the vortex shedding should exceed the energy dissipation of the acoustic mode.

4. **Turbulence Induced Vibrations (TIV)** : In this case the excitation of the structure is due to the random pressure fluctuation acting on the fluid-structure interface. These fluctuations can be generated locally by the fluid (near field excitation) or produced due to far field turbulence, i.e. the turbulence induced by other structures in front of the fuel rod. This phenomenon is the principal excitation mechanism in axial flow situations where flow separation does not occur.

Figure 1.3 above shows the occurrence of the aforementioned excitation mechanisms in different parts of the reactors and their relative importance. Another way to classify fluid-structure interaction excitation mechanisms given by Weaver et al. (2000) is based on how they are produced. The categories under this classification are listed below.

1. **Extraneously Induced Excitation**: This is caused by fluctuations in flow velocities or pressure that are independent of any instability due to structural movement except the added mass and fluid damping effects. The exciting force is mostly random but may also be periodic.

2. **Instability Induced Excitation**: In this mechanism the instability is intrinsic to the flow system created by the structure being considered. An example of this would be vortex induced vibrations. There is also a possibility of control mechanisms that can strengthen the excitation such as resonance and fluid-elastic feedback. An example of this is lock-in where the vortex shedding frequency matches the natural frequency of the the structure causing resonance. In case of rotating structures such as ocean drills, the lock in phenomenon can even occur at frequencies other than the natural frequency of the structure.

3. **Movement Induced Excitation**: This occurs due to fluctuating forces that arise due to the movement of a vibrating body. These type of vibrations are thus aptly named self excited.

Another way of classification was proposed by Weaver (1976) which is related to the nature of vibrations, (a) forced vibrations induced by turbulence, (b) self-controlled vibrations, for these vibrations some periodicity exists in the flow field which is independent of the movement of the structure and (c) self-excited vibrations. Blevins (1990) uses a phenomenological way of classification, grouping the vibrations as induced by (a) steady flow and (b) unsteady flow.

1.3 Research Objective

Being able to predict Flow Induced Vibrations plays an important role in (re)designing a nuclear plant as these can have detrimental effects on the structural components interacting with the fluids such as heat exchangers, boilers and fuel rods. Of all the possible types of excitations, simulating Turbulence Induced Vibrations is a particularly challenging problem for nuclear reactor applications and is the main focus of this thesis. As the source of excitation in such vibrations are the random turbulent fluctuations in the flow field, the fluid solver used for such simulations must be able to capture such fluctuations. Existing fluid solvers based on LES and DNS are capable of resolving these fluctuations. However such solvers are not suitable for industrial problems especially with high Reynolds numbers as they are computationally very expensive, especially for FSI applications where marching through a single coupled time step involves executing the fluid solver multiple times. A possible way to economically tackle this problem would be to synthetically model the turbulent fluctuations. The main goal of the current research is to *quantitatively evaluate the efficacy of using synthetic turbulent fluctuations for simulating Turbulence Induced Vibrations.*

1.4 Thesis Outline

In Chapter 2, the governing equations for both the fluid and the structural domain have been summarized. An overview of the Finite Volume Methodology used in OpenFOAM is also presented. This is followed by the description of the coupling conditions used at the fluid-structure interface. Finally the coupling algorithm used in this study is described. Chapter 3 presents the RANS methodology to describe turbulent flows. An approach to model the turbulent velocity and pressure fluctuations fields using known parameters from a RANS simulations is also described in detail. The coupled FSI solver is initially validated with a a numerical and experimental benchmark, as described in Chapter 4. Finally the efficacy of using the modeled fluctuation field to excite the structure in case of turbulence induced vibrations is verified in Chapter 5. Chapter 6 summarizes the work and provides some conclusions and suggestions for future work.

Chapter 2

Numerical Methodology

Every numerical simulation is based on a mathematical model that tries to describe the physics of the phenomenon being studied. When considering fluid structure interaction using a partitioned approach, this involves describing the equations governing the fluid domain, the structural domain and the ways to couple them both. This chapter provides a brief overview of the equations governing fluid dynamics and structural dynamics. Finite Volume method is used to discretize the fluid domain, and various aspects of this methodology are presented.

2.1 Frames of Reference

While observing any physical phenomena, the choice of the point of view by the observer heavily influences the form of observations being made. Although, the phenomena being observed is independent of the frame of reference of the observer, a suitable choice can simplify the analysis, making it easier to interpret. An example of this would be the choice made by the astronomer Copernicus to analyze the trajectories of the planets keeping the sun as the center instead of earth. This small change in frame of reference simplified the complicated motion of the planets to just ellipses. The two points of view typically used in continuum mechanics are *Lagrangian* and the *Eulerian* approach. The point of view particularly suitable for FSI is the *Arbitrary Lagrangian-Eulerian* approach. These three are briefly describe below,

Lagrangian Approach

The frame of reference is fixed to the material domain in this approach. The frame of reference moves according to the movement or deformation of the domain. This approach is often used in structural mechanics as it allows implicit treatment of moving boundaries and defines a property history to each material point.

Eulerian Approach

In the Eulerian approach the frame of reference is fixed to a particular spatial location regardless of the movement of the material being observed. Thus to measure the change in any given property f over time at a given location $\boldsymbol{x}$, one must add the change of the property at that location with time and the convective transport of neighboring material to that location with a material velocity $\boldsymbol{v}$. This change is often taken care by the material derivative,

$$\frac{df}{dt} \coloneqq \frac{\partial f}{\partial t} + (\mathbf{v} \cdot \nabla) f. \tag{2.1}$$

The advantage of using this approach is that it can handle any arbitrary deformation, which is why it is majorly used in fluid dynamics.

Arbitrary Lagrangian-Eulerian Approach

The Arbitrary Lagrangian-Eulerian (ALE) approach allows to move the frame of reference independent of the material motion. Hence the mesh can be moved independent of the material motion. The fluid mesh velocity is chosen in such a way that a Lagrangian behavior is obtained at the fluid structure interface, while the computational mesh in the interior of the fluid domain is moved using suitable mesh movement or smoothening techniques to balance out the distortions at the interface.

2.2 Fluid Dynamics

The field of fluid dynamics is categorized by types of flow, which also determines the governing equations. These categories of flow are compressible or incompressible flow, viscous or inviscid flow and laminar or turbulent flow. A flow is considered incompressible if the density of the respective fluid is constant (or nearly constant) or if the speed of sound in the fluid is large compared to the velocity of the fluid (which is the case for flows with Mach number less than 0.3). Such flows are highly resistant to compressive forces. Viscosity of the fluid determines its rate of deformation given a certain amount of shear. Inviscid flows are characterized by low viscosity and nearly negligible shear forces. Turbulent flows are characterized by highly irregular flow patterns in space and time, that occur when several flow parameters (summarized by Reynolds Number) exceed a certain threshold. The equations of fluid dynamics are obtained by conservation of mass, momentum and energy (for compressible flows). In the following section conservation of mass and momentum is discussed, leaving out conservation of energy as compressible flows is not a focus of this thesis.

Conservation of Mass

Conservation of mass states that the total mass of fluid in a closed system is constant over time and results in the continuity equation,

$$\frac{\partial \rho}{\partial t} + \rho \nabla \cdot (\mathbf{U}) + (\mathbf{U} \cdot \nabla)\rho = 0 \tag{2.2}$$

where $\mathbf{U}$ is the velocity vector and ρ is the density of the fluid. For an incompressible fluid flow, the partial derivative of ρ w.r.t time and space vanish. Hence, the above can be written as

$$\nabla \cdot \mathbf{U} = 0 \tag{2.3}$$

Conservation of Momentum

The conservation of momentum is a consequence of Newton's second law stating that the change in momentum of a system is due to an external force $\mathbf{F}$ acting on it. This above law can be written as,

$$\rho\left(\frac{\partial \mathbf{U}}{\partial t} + (\mathbf{U} \cdot \nabla)\mathbf{U}\right) = -\nabla p + \nabla \cdot \tau + \rho \mathbf{F} \tag{2.4}$$

where p is the pressure field and τ is the viscous stress tensor which in turn can be written using the following constitutive law for Newtonian fluids

$$\tau_{ij} = \mu\left(\frac{\partial U_i}{\partial x_j} + \frac{\partial U_j}{\partial x_i} - \frac{2}{3}\delta_{ij}\frac{\partial U_k}{\partial x_k}\right) \tag{2.5}$$

where μ is the viscosity of the fluid. For an incompressible flow, the last term of Eq. (2.5) vanishes and the conservation of momentum can be written as

$$\rho\Big(\frac{\partial \mathbf{U}}{\partial t} + (\mathbf{U} \cdot \nabla)\mathbf{U}\Big) = -\nabla p + \mu \Delta \mathbf{U} + \rho \mathbf{F} \tag{2.6}$$

The equations of conservation of mass and conservation of momentum for fluids are together called the *Navier-Stokes* equations. The above derived equations are in Eulerian frame of reference. As the Arbitrary Lagrangian-Eulerian approach is used in FSI problems, the *Navier-Stokes* equations for ALE formulation have been shown below,

$$\begin{aligned} &\text{Compressible flow} && \frac{\partial \rho}{\partial t} + \rho \nabla \cdot (\mathbf{c}) + (\mathbf{c} \cdot \nabla)\rho = 0 \\ &\text{Incompressible flow} && \rho \nabla \cdot \boldsymbol{c} = 0 \end{aligned} \tag{2.7}$$

$$\begin{aligned} &\text{Compressible flow} && \rho\left(\frac{\partial \mathbf{U}}{\partial t} + (\mathbf{c} \cdot \nabla)\mathbf{U}\right) = -\nabla p + \nabla \cdot \tau + \rho \boldsymbol{F} \\ &\text{Incompressible flow} && \rho\Big(\frac{\partial \mathbf{U}}{\partial t} + (\mathbf{c} \cdot \nabla)\mathbf{U}\Big) = -\nabla p + \mu \Delta \mathbf{U} + \rho \mathbf{F} \end{aligned} \tag{2.8}$$

$\mathbf{c}$ is the convective velocity defined as $\mathbf{U}$-$\hat{\mathbf{U}}$, where $\mathbf{U}$ is the material velocity w.r.t. to the spatial domain and $\hat{\mathbf{U}}$ is the mesh velocity which is the velocity of the referential domain w.r.t to the spatial domain.

2.3 Structural Dynamics

Most structural mechanics applications are limited to comparatively small strains due to the risk of material failure, e.g. cracks. Therefore we deal with rather small displacements (compared to fluid dynamics), allowing the use of Lagrangian description of the kinematics. The deformation of an elastic, isotropic, homogeneous and incompressible structure is governed by Saint-Venant-Kirchhoff material model which is derived using the conservation of momentum using Lagrangian point of view. The resulting equation in the differential form is given as, (Wriggers, 2008)

$$\rho\Big(\frac{\partial^2 \boldsymbol{u}}{\partial t^2}\Big) = \nabla \cdot \boldsymbol{S} + \rho \boldsymbol{f} \tag{2.9}$$

where $\boldsymbol{u}$ is the displacement field, ρ is the solid density, $\boldsymbol{f}$ consists of body forces and $\boldsymbol{S}$ is the 2nd Piola-Kirchhoff stress tensor which models surface forces.

2.4 Finite Volume Discretization

The goal of any discretization technique is to transform a partial differential equation into a set of corresponding algebraic equations. Solving this algebraic system provides the solution to the partial differential equation at certain discrete locations in space and time. The discretization procedure is divided into three parts spatial discretization, temporal discretization and equation discretization (Hirsch, 2007). The *spatial discretization* involves splitting the computational domain into smaller cells giving the co-ordinates of the points where the solution will be approximated and also a description of the computational boundary. *Temporal discretization* is used in transient simulation where the time duration of the simulation is broken down into discrete time intervals. *Equation discretization* involves generating a system of algebraic equations from the governing partial differential equations.

2.4.1 Solution Domain Discretization

In the Finite Volume Methodology the space is discretized into smaller control volumes. These volumes do not overlap with one another and fill up the entire domain. Fig. 2.1 shows a typical control volume (P) along with a neighboring cell (N). The computational point (P) for each control volume is located at the centroid of the cell, defined as

$$\int_{V_p} (\mathbf{x} - \mathbf{x}_p) dV = 0 \tag{2.10}$$

The control volume is bounded by flat faces on all sides and each face is shared with one neighboring control volume. The control volume shape can be any general polyhedron. The face area vector $\mathbf{S}$ is normal to the shared face between the 2 adjacent cells and has a magnitude equal to the area of the face. The vector $\mathbf{d}$ represents the distance between the center of

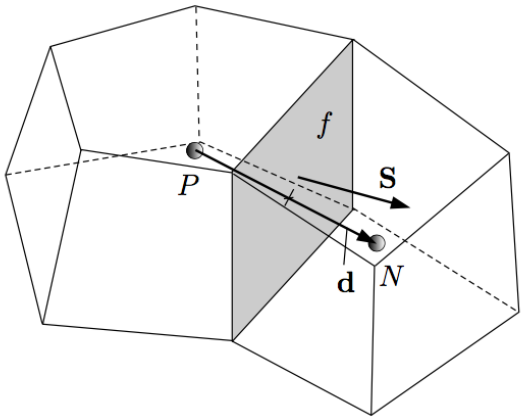

Figure 2.1: Computational cell (control volume) in Finite Volume Methodology (Rusche, 2003)

one cell (P) and the center of a neighboring cell center (N). A 'collocated' grid arrangement is commonly used, where the variables are stored at cell centers. The occurrence of oscillations in the solution field due to pressure-velocity decoupling in a collocated grid can be corrected using the Rhie and Chow interpolation (Rhie and Chow, 1983).

2.4.2 Equation Discretization

Instead of showing the discretization for each PDE involved, a general transport equation for any scalar ϕ given by,

$$\underbrace{\frac{\partial \rho\phi}{\partial t}}_{\text{temporal derivative}} + \underbrace{\nabla\cdot(\rho\mathbf{U}\phi)}_{\text{convection term}} - \underbrace{\nabla\cdot(\rho\Gamma\nabla\phi)}_{\text{diffusion term}} = \underbrace{S_\phi(\phi)}_{\text{source term}} \tag{2.11}$$

is used to describe the discretization procedure. In the above equation ρ, $\mathbf{U}$, Γ and $S_\phi(\phi)$ represent the density, velocity, diffusivity and the source term respectively. The individual terms in the above equation represent the change in any given scalar (ϕ) due to time rate of change (temporal derivative), the efflux due to convection (convection term), transport rate due to diffusion (diffusion rate) and the production/destruction of the scalar (source term). The finite volume discretization of Eq. 2.11 is obtained by integrating this equation over a control volume V_p and over a time interval (Δt) as shown below,

$$\begin{aligned}\int_t^{t+\Delta t}\Big[\int_{V_p}\frac{\partial\rho\phi}{\partial t}dV + \int_{V_p}\nabla\cdot(\rho\mathbf{U}\phi)dV - \int_{V_p}\nabla\cdot(\rho\Gamma\nabla\phi)dV\Big]dt \\ = \int_t^{t+\Delta t}\Big(\int_{V_p}S_\phi(\phi)dV\Big)dt\end{aligned} \tag{2.12}$$

The discretization of the terms in above equation is examined term by term in the next sections.

2.4.2.1 Convection Term

The discretization of the convection term is obtained using the Gauss's theorem as,

$$\int_{V_p} \nabla \cdot (\rho \mathbf{U} \phi) dV = \sum_f \mathbf{S} \cdot (\rho \mathbf{U} \phi)_f = \sum_f \mathbf{S} \cdot (\rho \mathbf{U})_f \phi_f = \sum_f F \phi_f \tag{2.13}$$

where the subscript f means that the quantity is calculated at the middle of the cell face, $\mathbf{S}$ is the outward pointing surface area vector and F represents the mass flux through a given face f. To calculate the above terms the values of the variables ρ, $\mathbf{U}$ and ϕ need to be evaluated at the cell faces whereas originally these are stored at the cell centers. Hence an interpolation technique is required to calculate the aforementioned terms. This can be done using any convection differencing schemes. Assuming a linear variation of the interpolated quantity (ϕ) between the 2 neighboring cells (P and N) to a face (f), the face value can be calculated as,

$$\phi_f = f_x \phi_P + (1 - f_x) \phi_N. \tag{2.14}$$

where f_x is the interpolation factor defined as ratio of distance between the face and the cell center N ($\overline{fN}$) and the distance between the face and the cell center P ($\overline{fP}$) i.e. $f_x = \overline{fN}/\overline{fP}$. This differencing scheme is second order accurate and is known as the *Central Differencing* scheme. It has however been reported to cause unphysical oscillations in the computed solution for convection-dominated flows (Hirsch, 2007) leading to unbounded solutions. Using an *Upward* differencing scheme can guarantee a bounded solution as in this approximation the face value of ϕ is taken as the value of the cell center in the upstream direction. However this method distorts the solution by introducing numerical diffusion. Many other schemes that combine upward and central differencing schemes depending on the variation rate of the quantity ϕ for individual faces have been proposed to combine accuracy and boundedness Jasak (1996).

2.4.2.2 Diffusion Term

The diffusion term is discretized in the same way as the convection term using Gauss's theorem,

$$\int_{V_p} \nabla \cdot (\rho \Gamma \nabla \phi) dV = \sum_f \mathbf{S} \cdot (\rho \Gamma \nabla \phi)_f = \sum_f (\rho \Gamma)_f \mathbf{S} \cdot (\nabla \phi)_f \tag{2.15}$$

In case of orthogonal meshes the vector $\mathbf{d}$ and $\mathbf{S}$ are parallel (shown in Fig. 2.1). Hence, the face normal gradient ($\mathbf{S} \cdot \nabla \phi$) can be approximated as,

$$\mathbf{S} \cdot (\nabla \phi)_f = |\mathbf{S}| \frac{\phi_N - \phi_P}{|\mathbf{d}|} \tag{2.16}$$

However in case of non-orthogonal meshes, a correction term is introduced as shown below,

$$\mathbf{S} \cdot (\nabla \phi)_f = \underbrace{|\mathbf{\Delta}| \cdot (\nabla \phi)_f}_{\text{orthogonal contribution}} + \underbrace{\mathbf{k} \cdot (\nabla \phi)_f}_{\text{non-orthogonal contribution}} \tag{2.17}$$

where $\mathbf{\Delta}$ and $\mathbf{k}$ are vectors that are determined by using suitable non-orthogonality treatments Jasak (1996).

2.4.2.3 Source Term

Any terms of a governing equation that can't be written as temporal derivative, convective or diffusive term can be written as the source terms. The source terms are usually linearized as shown in Patankar (1980):

$$S_\phi = Su + Sp\phi \tag{2.18}$$

Using the above form the volume integral can be written as,

$$\int_{V_p} S_\phi(\phi) dV = SuV_p + SpV_p\phi \tag{2.19}$$

2.4.2.4 Temporal Discretization

Substituting the volume integrals as previously calculated for the standard transport equation into Eq. (2.12), we get the semi-discretized form,

$$\int_t^{t+\Delta t} \Big[\Big(\frac{\partial \rho\phi}{\partial t}\Big)_P V_P + \sum_f F\phi_f - \sum_f (\rho\Gamma)_f \mathbf{S}\cdot(\nabla\phi)_f\Big] dt = \int_t^{t+\Delta t} (SuV_p + SpV_p\phi) dt. \tag{2.20}$$

The time derivative and the integrals in the above equation can be written as,

$$\begin{aligned}
\Big(\frac{\partial \rho\phi}{\partial t}\Big)_P &= \frac{\rho_P^n\phi_P^n - \rho_P^0\phi_P^0}{\Delta t} \\
\text{Crank-Nicolson}: \int_t^{t+\Delta t} \phi(t) dt &= \frac{1}{2}(\phi^0 + \phi^n)\Delta t \\
\text{Explicit-Euler}: \int_t^{t+\Delta t} \phi(t) dt &= (\phi^0)\Delta t \\
\text{Implicit-Euler}: \int_t^{t+\Delta t} \phi(t) dt &= (\phi^n)\Delta t
\end{aligned} \tag{2.21}$$

Substituting the above in Eq. (2.20), we get the *Crank-Nicolson* time integration method, as shown below

$$\begin{aligned}
\frac{\rho_P^n\phi_P^n - \rho_P^0\phi_P^0}{\Delta t} V_P + \frac{1}{2}\sum_f F\phi_f^n - \frac{1}{2}\sum_f (\rho\Gamma)_f \mathbf{S}\cdot(\nabla\phi)_f^n \\
\frac{1}{2}\sum_f F\phi_f^0 - \frac{1}{2}\sum_f (\rho\Gamma)_f \mathbf{S}\cdot(\nabla\phi)_f^0 \\
= SuV_P + \frac{1}{2}SpV_P\phi_P^n + \frac{1}{2}SpV_P\phi_P^0.
\end{aligned} \tag{2.22}$$

2.4.3 System of Algebraic Equations

The unknown variable in Eq. (2.22) is the value of ϕ_P at the next time step n. The values of ϕ and $\nabla\phi$ at both the current and previous time steps are required to solve this system.

Also the face values of ϕ and $\nabla\phi$ depends on the cell values on either side of the face. Hence Eq. (2.22) can be rewritten as,

$$a_P\phi_P^n + \sum_N a_N\phi_N^n = R_p \tag{2.23}$$

The above equation is then created for every control volume in the domain to get an overall system of equations which can be written as,

$$[A][\phi] = [R] \tag{2.24}$$

Solving the above system gives the ϕ field for the domain at the next time step. Such a system can be either solved directly or using iterative techniques. However iterative procedures are computationally less expensive and are hence commonly used (Muzaferija, 1994).

2.5 Coupling of Fluid and Structural domains

This section discusses the coupling conditions at the fluid-structure interface. In this section the subscript **F** denotes the fluid domain, whereas the subscript **S** denotes the structural domain. A schematic of the coupling interface has been shown in Fig. 2.2 where Ω_F, Ω_S represent the fluid and the structure domain, while Γ_{FS} is the overlapping interface of both the domains. Also $\mathbf{n}$ is the normal vector to either domain.

- *Kinematic Boundary Condition*: This condition imposes that the displacement and the velocity at the interface should be same for both the fluid as well as the structural domain. The equality of velocity stems from the fact, that under the assumption of no slip, the fluid molecules at the interface would be bound to the structure and hence have the same velocity as the structure. The equality of displacement is due to the fact that the fluid and structure fill up the domains up to the interface and there is no overlapping. The conditions are give as

$$\boldsymbol{x}_F = \boldsymbol{u}_S, \quad \boldsymbol{v}_F = \frac{\partial \boldsymbol{u}_S}{\partial t} \quad \text{at } \Gamma_{FS} \tag{2.25}$$

- *Dynamic Boundary Condition*: This boundary condition imposes the fact that the traction at the interface of the structure is in equilibrium with that on the fluid side. This is basically a force balancing operation. The condition is given by,

$$\boldsymbol{\sigma}_F \cdot \boldsymbol{n}_F = \boldsymbol{\sigma}_S \cdot \boldsymbol{n}_S \quad \text{at } \Gamma_{FS} \tag{2.26}$$

2.5.1 Coupling Algorithm

The **I**nterface **Q**uasi-**N**ewton with **I**nverse Jacobian from a **L**east **S**quares model (IQN-ILS) is a well validated coupling algorithm for strongly coupled problems and can be used for

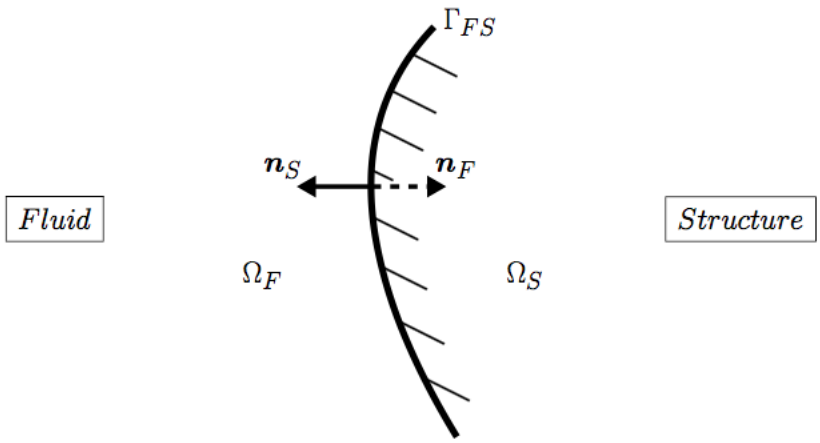

Figure 2.2: Schematic of the interface of a fluid and structural domain Gatzhammer (2014)

black-box solvers Degroote (2013). IQN-ILS is used as the coupling algorithm for the simulation performed in this thesis. Hence, an overview of this algorithm (amended from Degroote (2013)) is provided in this section. For further discussion, the fluid and the structural solver are represented as operators $\mathbf{F}$ and $\mathbf{S}$ respectively. The input-output variables for these operators are the kinematic values $\mathbf{x}$ which comprise of displacement and velocities, and the dynamic values $\mathbf{y}$ comprising of forces and stresses. Using a Dirichlet-Neumann decomposition, the flow equations are solved for a given displacement of the fluid-structure interface (Dirichlet boundary condition) and the structural equations are solved for a given traction distribution on the interface (Neumann boundary condition), the solvers can be written as,

$$\mathbf{y} = \mathbf{F}(\mathbf{x}) \tag{2.27}$$

$$\mathbf{x} = \mathbf{S}(\mathbf{y}) \tag{2.28}$$

The traction on the interface $\mathbf{y}$ can be eliminated from the above set of equations, resulting in an equation with only kinematic variables (interface displacement in this case)

$$\mathbf{S} \circ \mathbf{F}(\mathbf{x}) - \mathbf{x} = 0 \tag{2.29}$$

Introducing a residual operator $\mathbf{R}$ defined as

$$\mathbf{R} = \mathbf{S} \circ \mathbf{F}(\mathbf{x}) - \mathbf{I} \tag{2.30}$$

with $\mathbf{I}$ being the identity operator of the required dimensions, yields a smaller equation with $\mathbf{x}$ as the unknown

$$\mathbf{R}(\mathbf{x}) = 0 \tag{2.31}$$

The goal is to minimize this residual or to find the zero of the above equation using Newton-Raphson iterations. The Jacobian of $\mathbf{R}$ with respect to x is further denoted by $\mathbf{R}'$ and in each Newton iteration a linear system

$$\mathbf{R}'^{k} \Delta \mathbf{x}^{k} = -\mathbf{R}(\mathbf{x}^{k}) \tag{2.32}$$

is solved with $\Delta\ \mathbf{x}^k = \mathbf{x}^{k+1}$ - $\mathbf{x}^k$. We need to approximate the Jacobian because the exact Jacobian of $\mathbf{R(x)}$ is unknown as both $\mathbf{F}$ and $\mathbf{S}$ are taken as black box functions and are therefore unavailable. In each iteration the residual vector is calculated as the difference between the output of the structural solver ($\tilde{\mathbf{x}}^k$) and the input of the flow solver (x_f^k) i.e.

$$\mathbf{r}^k = \mathbf{R}(\mathbf{x}^k) = \mathbf{S} \circ \mathbf{F}(\mathbf{x}^k) - \mathbf{x}^k = \tilde{\mathbf{x}}^k - \mathbf{x}^k \tag{2.33}$$

The linear system of equations (2.32) has the same dimensions as the number of nodes at the fluid-structure interface, and this has to be solved in each iteration. Although the number of nodes at the fluid-structure interface is considerably lower than the individual flow or structure domain, the Jacobian matrix ($\mathbf{R'}$) is usually dense. Hence the solution of this system of linear equations is computationally expensive for large simulations. Therefore, it is more advantageous to approximate the inverse of this Jacobian using the least squares method.In this way the system of linear equations (2.32) can be rewritten as

$$\mathbf{x}^{k+1} = \mathbf{x}^k + \widehat{(\mathbf{R'}^k)^{-1}}(-\mathbf{r}^k) \tag{2.34}$$

It can be seen from the above equation (2.34) that the approximation for the inverse of the Jacobian does not have to be calculated explicitly. Instead we need to calculate the product of this inverse Jacobian with the vector $-\mathbf{r}^k$. This vector is the difference between the desired residual i.e. 0 and the current residual $\mathbf{r}^k$ and is denoted as $\Delta\mathbf{r} = 0$ - $\mathbf{r}^k = -\mathbf{r}^k$. The matrix-vector product is calculated from the information obtained during the previous iterations. The vectors $\tilde{\mathbf{x}}$ and $\mathbf{r}$ are available from the previous iterations, giving a set of residual vectors

$$\mathbf{r}^k, \mathbf{r}^{k-1}, \ldots, \mathbf{r}^1, \mathbf{r}^0 \tag{2.35}$$

and also a corresponding set of displacement vectors $\tilde{\mathbf{x}}$

$$\tilde{\mathbf{x}}^k, \tilde{\mathbf{x}}^{k-1}, \ldots, \tilde{\mathbf{x}}^1, \tilde{\mathbf{x}}^0 \tag{2.36}$$

The difference between the vectors from the current iterations and the previous iteration is calculated repeatedly for every iteration, thus giving us the following vectors

$$\begin{aligned} \Delta\mathbf{r}^{k-1} &= \mathbf{r}^k - \mathbf{r}^{k-1} \\ \Delta\tilde{\mathbf{x}}^{k-1} &= \tilde{\mathbf{x}}^k - \tilde{\mathbf{x}}^{k-1} \end{aligned} \tag{2.37}$$

This yield another set of vectors $\Delta\mathbf{r^i}$

$$\Delta\mathbf{r}^k, \Delta\mathbf{r}^{k-1}, \ldots, \Delta\mathbf{r}^1, \Delta\mathbf{r}^0 \tag{2.38}$$

and also a corresponding set of vectors $\Delta\tilde{\mathbf{x}}^i$

$$\Delta\tilde{\mathbf{x}}^k, \Delta\tilde{\mathbf{x}}^{k-1}, \ldots, \Delta\tilde{\mathbf{x}}^1, \Delta\tilde{\mathbf{x}}^0 \tag{2.39}$$

Each $\Delta\mathbf{r}^i$ corresponds to a $\Delta\tilde{\mathbf{x}}^i$ and these vectors are stored as columns of the matrices

$$\mathbf{V}^k = [\Delta\mathbf{r}^{k-1} \quad \Delta\mathbf{r}^{k-2} \quad \ldots \quad \Delta\mathbf{r}^1 \quad \Delta\mathbf{r}^0] \tag{2.40}$$

$$\mathbf{W}^k = [\Delta\tilde{\mathbf{x}}^{k-1} \quad \Delta\tilde{\mathbf{x}}^{k-2} \quad \dots \quad \Delta\tilde{\mathbf{x}}^{1} \quad \Delta\tilde{\mathbf{x}}^{0}] \tag{2.41}$$

Due to similarity between consecutive time steps, information from previous time steps can also be combined with the matrices $\mathbf{V}^k$ and $\mathbf{W}^k$, giving (assuming at least q time steps have been performed)

$$\mathbf{V}^k = [\Delta\mathbf{V}^k \quad \Delta\mathbf{V}^n \quad \dots \quad \Delta\mathbf{V}^{n-q+2} \quad \Delta\mathbf{V}^{n-q+1}] \tag{2.42}$$

$$\mathbf{W}^k = [\Delta\mathbf{W}^k \quad \Delta\mathbf{W}^n \quad \dots \quad \Delta\mathbf{W}^{n-q+2} \quad \Delta\mathbf{W}^{n-q+1}] \tag{2.43}$$

The convergence of the problems is generally accelerated by including information from the previous time steps upto a certain number of time steps and can slow down again if even greater number of time steps are re-used. The optimal value of time steps reused (q) is problem dependent but the convergence of coupling iterations does not change significantly near the optimum value. The number of columns in $\mathbf{V}^k$ and $\mathbf{W}^k$ is indicated with v and is usually much smaller than the number of rows u. The vector $\Delta\mathbf{r}$ = 0 - $\mathbf{r}^k$ is approximated as the linear combination of the known $\Delta\mathbf{r}^i$

$$\Delta\mathbf{r} \approx \mathbf{V}^k\mathbf{c}^k \in \mathbb{R} \tag{2.44}$$

with $\mathbf{c}^k \in \mathbb{R}^{v\times 1}$ the coefficients of decomposition. Since v is less than u, this system is overdetermined for the coefficients of decomposition $\mathbf{c}^k$, hence the least squares solution to this system is calculated. For this the economy-size QR-decomposition of $\mathbf{V}^k$ is calculated using Householder transformations (Golub and Van Loan, 2012)

$$\mathbf{V}^k = \mathbf{Q}^k\mathbf{R}^k \tag{2.45}$$

Now the coefficient $\mathbf{c}^k$ can be determined by solving

$$\mathbf{R}^k\mathbf{c}^k = \mathbf{Q}^{kT}\Delta\mathbf{r} \tag{2.46}$$

The $\Delta\tilde{\mathbf{x}}$ that corresponding to $\Delta\mathbf{r}$ are calculated in a similar way as a linear combination of known $\Delta\tilde{\mathbf{x}}^i$

$$\Delta\tilde{\mathbf{x}} = \mathbf{W}^k\mathbf{c}^k \tag{2.47}$$

Using Eq. (2.33), we can write

$$\Delta\mathbf{r} = \Delta\tilde{\mathbf{x}} - \Delta\mathbf{x} \tag{2.48}$$

Using Eq. (2.48) and (2.47), we get

$$\Delta\mathbf{x} = \mathbf{W}^k\mathbf{c}^k - \Delta\mathbf{r} \tag{2.49}$$

Using the fact $\Delta\mathbf{r}$ = -$\mathbf{r}^k$, we can write

$$\Delta\mathbf{x} = \widehat{(\mathbf{R}'^k)^{-1}}(-\mathbf{r}^k) = \mathbf{W}^k\mathbf{c}^k + \mathbf{r}^k \tag{2.50}$$

The overall algorithm has been summarized in Algorithm 1.

Algorithm 1: IQN-ILS algorithm Degroote (2013)

k=0;
$\tilde{\mathbf{x}}^0 = \mathbf{S} \circ \mathbf{F}(\boldsymbol{x}^0)$;
$\mathbf{r}^0 = \tilde{\mathbf{x}}^0 - \mathbf{x}^0$;
while $\|\mathbf{r}^k\|_2 > \epsilon_0$ **do**
  if *k = 0 and (q = 0 or n = 0)* **then**
    $\mathbf{x}^{k+1} = \mathbf{x}^k + \omega \mathbf{r}^k$;
  else
    construct $\mathbf{V}^k$ and $\mathbf{W}^k$;
    calculate Q-R decomposition $\mathbf{V}^k = \mathbf{Q}^k \mathbf{R}^k$;
    solve $\mathbf{R}^k \mathbf{c}^k = \mathbf{Q}^{kT} \Delta \mathbf{r}$;
    $\mathbf{x}^{k+1} = \mathbf{x}^k + \mathbf{W}^k \mathbf{c}^k + \mathbf{r}^k$;
  end
  $\tilde{\mathbf{x}}^{k+1} = \mathbf{S} \circ \mathbf{F}(\mathbf{x}^k)$;
  $\mathbf{r}^{k+1} = \tilde{\mathbf{x}}^{k+1} - \mathbf{x}^{k+1}$;
  k++ ;
end

2.6 Summary

This chapter reviewed and summarized the broad numerical concepts used in Fluid Structure Interaction problems. This includes the frame of reference that is most beneficial for FSI problems, the differential equations governing the phenomena being studied, the coupling criteria at the interface of two different domains, and the finite volume methodology. The IQN-ILS coupling algorithm for the partitioned approach is also discussed, as this is the coupling algorithm used in the framework of this thesis.

Chapter 3

Synthetic Modeling of Pressure Fluctuations

Most of the naturally occurring fluid flows are turbulent in nature. Turbulence can be defined as a state of continuous instability in a fluid flow. At high Reynolds number, flows described by the Navier-Stokes equations are extremely sensitive to initial conditions and disturbances and turbulence may be considered the chaotic response to these conditions. Turbulent flows are characterized by higher diffusivity and greater energy dissipation (Tennekes and Lumley, 1972). The range of scales involved in turbulent flows is very wide, ranging from smallest eddies (Kolmogorov scales) to eddies comparable to the size of the geometry. The range of these scales increases with Reynolds number.

Historically the analysis of turbulence has had three parallel movements, statistical, structural and deterministic (Chapman and Tobak, 1985). Reynolds put forth the *statistical* view point implying that limited practical information can be gained from studying the complex details of the flow and suggested the decomposition of the flow field into mean and fluctuating components. Experimental results of wall-bounded turbulent flows showing coherent structures and correlations between various spatial and temporal positions (Bernard and Wallace, 2002), led to the conclusion that turbulence may not be completely random leading to the *structural* movement. The *deterministic* movement analyzes the chaotic and complex flow patterns of a turbulent flow as a solution to the Navier-Stokes solutions. These solutions can replicate the sensitivity of the flow behavior to small disturbances and initial conditions.

There are three popular approaches of numerically simulating turbulence viz. Direct Numerical Simulation (DNS) , Large Eddy Simulation (LES) and Reynolds Averaged Navier-Stokes (RANS). In Direct Numerical Simulations, all the relevant scales of the fluid flow are resolved. This puts very high demands on the computational resources due to the required mesh resolution and the time step sizes involved, making it unsuitable for engineering problems. Despite these restrictions, DNS is a useful tool in turbulence research as it is often used to calibrate/evaluate computationally cheaper approaches. As in DNS every scale is explicitly evaluated, this method is categorized in the deterministic approach. In Large Eddy Simulations, the largest scales (super-grid scales) of the turbulent flow are resolved while the smaller scales

(sub- scales) are approximated using models. The idea behind this approach is that the large scale structures in a flow are influenced by the flow geometry and the boundary conditions hence need to be resolved, whereas, the smaller scales tend to be more homogeneous and isotropic, hence can be modeled. The third approach tackles the problem using a statistical view point using the RANS methodology. This involves separating the variable values in a flow field into the mean and the fluctuations around the mean, thus obtaining the governing equations for the mean quantities. As this approach is heavily used in engineering applications and forms the basis of the subsequent discussion, RANS has been briefly described in the next section.

3.1 RANS Methods

Reynolds Averaged Navier-Stokes (RANS) methods involve applying an averaging method to separate the flow variables into a mean and fluctuating component, and then derive the equations for mean flow variables using empirical models to replicate the effects of fluctuations on the mean field. Depending on how the mean of a variable is defined, the averaging procedure can be approached in three ways (Hinze, 1975):

1. Time averaging: averaging any variable (ϕ) at a fixed point in space, suitable for statistically stationary turbulence.
2. Spatial averaging: averaging any variable (ϕ) at a fixed instance of time, suitable for homogeneous turbulence.
3. Ensemble averaging: this is the most general form of averaging where any variable (ϕ) is averaged over a series of identical experiments

The ensemble averaging procedure is described as:

$$\phi(\boldsymbol{x}, t) = \overline{\phi}(\boldsymbol{x}, t) + \phi'(\boldsymbol{x}, t) \tag{3.1}$$

where $\overline{\phi}(\boldsymbol{x}, t)$ represents the mean value of ϕ whereas $\phi'(\boldsymbol{x}, t)$ shows the fluctuations in ϕ about the aforementioned described mean. The mean value is defined as,

$$\overline{\phi}(\boldsymbol{x}, t) = \lim_{N \to \infty} \frac{1}{N} \sum_{i=1}^{N} \phi_i(\boldsymbol{x}, t) \tag{3.2}$$

where N is the number of identical experiments. Fig. 3.1 shows three samples of velocity measured at a point and their ensemble average.

Rewriting the incompressible Navier-Stokes equations as described earlier in section 2.2, we get

$$\nabla \cdot \boldsymbol{U} = 0 \tag{3.3}$$

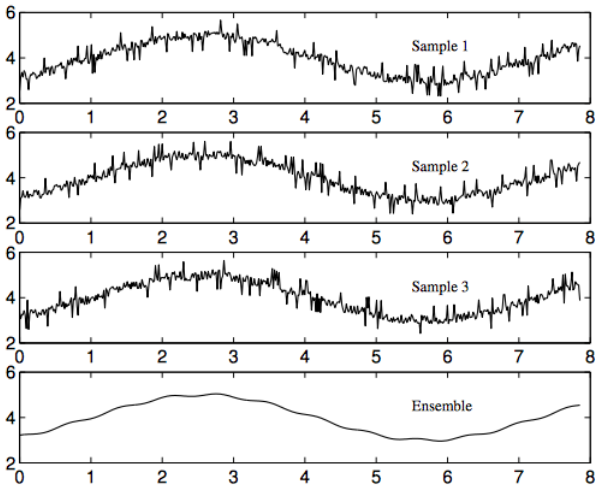

Figure 3.1: Ensemble average of 3 samples of velocity measured at a point in turbulent flow (Recktenwald, 2009)

$$\frac{\partial \boldsymbol{U}}{\partial t} + \nabla \cdot (\boldsymbol{U}\,\boldsymbol{U}) = \mathbf{g} - \nabla p + \nabla \cdot (\nu \nabla \boldsymbol{U}) \tag{3.4}$$

where, $\boldsymbol{U}$, p, ν and $\mathbf{F}$ are the velocity field, pressure , kinematic viscosity and the body force acting on the fluid. Applying the Reynolds averaging procedure as shown in Eqs. (3.1 and 3.2) to the above equations, the following averaged equations can be obtained.

$$\nabla \cdot \overline{\boldsymbol{U}} = 0 \tag{3.5}$$

$$\frac{\partial \overline{\boldsymbol{U}}}{\partial t} + \nabla \cdot (\overline{\boldsymbol{U}}\,\overline{\boldsymbol{U}}) = \mathbf{g} - \nabla \overline{p} + \nabla \cdot (\nu \nabla \overline{\boldsymbol{U}}) + \overline{\boldsymbol{U}'\boldsymbol{U}'} \tag{3.6}$$

It can be observed that the averaged equations for the mean flow are identical to the governing equations for instantaneous flow except for an additional term $\overline{\boldsymbol{U}'\boldsymbol{U}'}$. This term acts as an additional stress term and is called the Reynolds stress tensor. The averaging procedure creates additional unknown variables and no new governing equations. Hence the above set of equations are not enough to close to system. This is known as the *closure problem* in turbulence. This problem is still unsolved. Reynolds averaged turbulence modeling is used to express the Reynolds stress tensor in terms of known quantities to close the system. One of the most common approach used is the Boussinesq approximation (Boussinesq, 1877). This hypothesis was postulated by Boussinesq and relates the turbulence of the flow field to a *higher fluid viscosity*. The logic behind this assumption is the observation that higher turbulence leads to a more chaotic flow which makes the diffusion of any property such as heat more easier. Thus increasing the diffusion coefficient (molecular viscosity) of the fluids can help approximate this phenomenon. This increase in viscosity is the so called eddy or turbulent viscosity. The Boussinesq approximation is given as

$$\overline{\boldsymbol{U}'\boldsymbol{U}'} = \nu_t(\nabla \boldsymbol{U} + (\nabla \boldsymbol{U})^T) + \frac{2}{3}k\mathbf{I} \tag{3.7}$$

where $k = \frac{1}{2}\overline{\boldsymbol{U}' \cdot \boldsymbol{U}'}$ is the turbulent kinetic energy and ν_t is the kinematic eddy/turbulent viscosity. The Boussinesq hypothesis allows one to rewrite the Reynolds stress term in terms of known quantities but introduces two unknowns k and ν_t. In the $k-\epsilon$ turbulence model (Launder and Spalding, 1974), ν_t is expressed as a function of turbulent kinetic energy (k) and its dissipation rate (ϵ), giving the following equation,

$$\nu_t = C_\mu \frac{k^2}{\epsilon} \tag{3.8}$$

In RANS (Reynolds Averaged Navier Stokes) models the solution marches in time with a locally optimized time step for each cell. Although this gives a faster convergence to the steady state, the solution is not time accurate. However in Unsteady (U)-RANS models a global time step is used for each cell. Therefore if the time step is small enough, the unsteady behaviour of the mean quantities can be captured in principle. U-RANS models are widely used in industries as they are they are relatively cheaper and efficient in computing turbulent fluid flow properties. As these models compute time averaged quantities of the flow such as velocity, pressure and temperature, very little information on the fluctuating quantities is available. The useful turbulent quantities available are turbulent kinetic energy (K), the energy dissipation rate (ϵ) and Reynolds shear stress tensor.

De Ridder et al. (2013) numerically simulated the vibrations of a flexible brass cylinder in an axial water flow. The simulation setup replicates the experiments done by Chen and Wambsganss (1972). Initially the purely structural problem is solved to get the eigenmodes of the cylinder using a finite element solver while neglecting the damping in the structure. The brass cylinder is then deformed to a particular eigenmode such that the maximum displacement is scaled to unity. Then the fluid only steady state simulation is run while treating the interface as a rigid wall boundary. The final step comprises of running an unsteady FSI simulation to get the displacement history of the initially deformed structure. The modal characteristics of the brass cylinder are then studied by calculating parameters such as damping ratio and oscillation frequencies for various values of water inflow velocities. However, this method has a major drawback when applied to study turbulence induced vibrations which is usually the case for axial flows around structures. Any external excitation provided to the structure would eventually damp out due to lack of excitation from the fluid flow itself. This is due to the fact that the instantaneous velocity and pressure fluctuations are averaged in U-RANS models and hence heavily damped out. The next section discusses a procedure to calculate the velocity and pressure fluctuations using the known turbulence data found using U-RANS models.

3.2 Modeling the Synthetic Fluctuation Fields

For an incompressible flow field, the pressure fluctuations are related to the velocity fluctuations through the following Poisson's equations.

$$\frac{\partial^2 p'}{\partial x_i \partial x_i} = -\rho \left[2 \frac{\partial \overline{u_i}}{\partial x_j} \frac{\partial u_j'}{\partial x_i} + \frac{\partial^2}{\partial x_i \partial x_j} \left(u_i' u_j' - \overline{u_i' u_j'} \right) \right] \tag{3.9}$$

Kraichnan (1956) observed that the first term on the right hand side of Eq. (3.9) represents the mean shear turbulence interaction. This term is also called the rapid pressure fluctuation term as it varies quickly in response to changes in flow conditions and the second term on the right hand side represents the interaction of turbulence with itself. This term is called the slow pressure fluctuation term as it responds slowly to variation in flow field. The author also obtained a theoretical solution for the pressure fluctuation.

Chen (1985) derived a method to calculate root mean square pressure fluctuations and also worked out a transport equation for root mean square pressure fluctuations. The unknown terms in the above equation required additional modeling to close the system. The coefficients used for this modeling were calculated using the available experimental and Large-Eddy Simulation data.

In the work done by Senthooran (2002) the velocity fluctuations in the 3-D flow field are represented as a sum of discrete Fourier modes. To explain the concept used by Senthooran to model the velocity fluctuations, the concept of energy cascade is briefly explained first.

3.2.1 Energy Cascade

The energy cascade is a concept central to the discussion about turbulent flows which describes the process where the kinetic energy from the larger eddies in the flows is transferred to increasingly smaller eddies. Although some energy dissipation due to viscosity happens at all length scales, the larger eddies are majorly inviscid and most of their energy is transferred to increasingly smaller scales where this energy is eventually dissipated due to viscous forces and converted into thermal energy. This process of energy transfer to smaller scales is poetically described by Richardson (2007) as

Big whorls have little whorls
That feed on their velocity,
And little whorls have lesser whorls
And so on to viscosity.

Higher Reynolds number lead to a greater range of eddy scales. Usually the energy distribution across all the scales is visualized with the turbulence kinetic energy spectrum. The energy spectrum $E(\kappa)$ is defined using the turbulent kinetic energy (k) as,

$$k = \int_0^\infty E(\kappa) d\kappa \tag{3.10}$$

where κ is he wavenumber associated with any particular eddy scale and is inversely proportional to the eddy length scale. Hence, smaller wavenumbers correspond to larger eddies and vice versa. The above equation implies that the total turbulent kinetic energy is equal to the summation of energy contained at all eddy length scales. A typical energy spectrum plot for a turbulent flow is shown in Fig. 3.2.

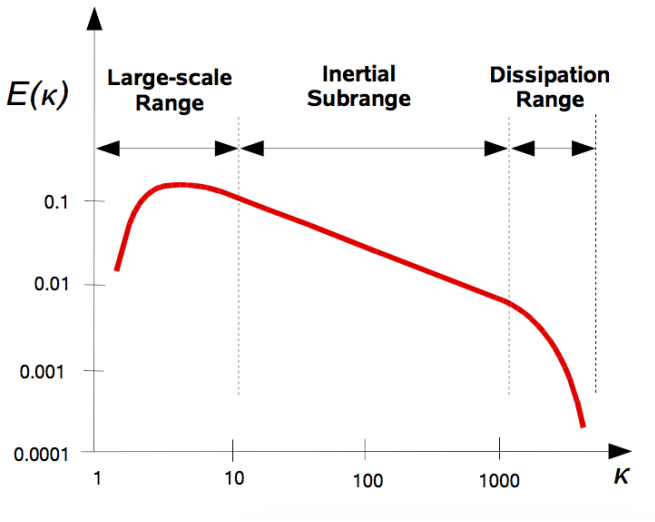

Figure 3.2: Energy spectrum for a turbulent flow field

Kolmogorov (1941) introduced the concept of scale separation which states the dynamics of eddies at the smallest scale are statistically independent of that of the larger ones. He also postulates that in case of equilibrium for turbulent flow, the rate of energy dissipation at the smallest scales to due to viscosity is equal to the rate of energy supplied from the largest scales. Kolmogorov also defined an intermediate scale which is independent of the dynamics of both the aforementioned scales. Each of these three scales are shown in Fig. 3.2 and are briefly describe below:

1. **Large-scale range**: These are the largest scales in the flow and are highly influenced by the flow conditions and geometry. These scales are responsible for turbulence production as they extract energy from the mean flow and transfer it over to smaller scales.

2. **Inertial-subrange**: This scale exists if the Reynolds number of the flow field is high enough. The eddies in this range extract energy from higher scales but the dissipation due to viscosity is minimal.

3. **Dissipation range**: In this range the dynamics of the eddies are dominated by viscosity (ν) and the rate of energy transfer (ϵ) from larger scales. The turbulent eddies at this scale are independent of the characteristics of the larger scales in the flow, are unaffected by boundary conditions and are hence assumed to be isotropic. Using dimensional analysis the scales associated with this range can be calculated as,

$$\begin{aligned} \text{kolmogorov length scale} \quad & \eta = \left(\frac{\nu^3}{\epsilon}\right)^{1/4} \\ \text{kolmogorov time scale} \quad & \tau = \left(\frac{\nu}{\epsilon}\right)^{1/2} \\ \text{kolmogorov velocity scale} \quad & v = (\nu\epsilon)^{1/4} \end{aligned} \tag{3.11}$$

3.2.2 Velocity Fluctuation Modeling as Fourier Series

The velocity fluctuations are modeled by expanding it with a Fourier series. Each term of the Fourier series models the fluctuation field due to each eddy length scale. The range of eddy lengths is continuous in a turbulent regime, therefore it is discretized into a select number of modes or wave numbers as shown below:

$$u'(x,t) = \sum_{n=1}^{N} \tilde{u}_n \cos\left[k_n \cdot (x - tu_c) + \psi_n + \omega_n t\right]\sigma_n \tag{3.12}$$

where $\tilde{u}_n$ is the amplitude, ψ_n is the phase and σ_n is the unit direction vector of the n^{th}mode associated with the wave vector k_n, ω_n is the characteristic angular frequency and u_c is the convection velocity respectively.

The wave vector (k_n) is defined as the inverse of the eddy length scale in 1-D. For a 3 dimensional space the wave vector is defined in form of a 3 component vector. The direction vector (σ_n) is a unit vector that specifies the direction of each component of the velocity fluctuation amplitude ($\tilde{u}_n$) in 3 dimensions. The relationship between the 2 quantities mentioned above is described below. For an incompressible flow, the continuity equation can be written as:

$$\nabla \cdot \boldsymbol{U} = 0 \tag{3.13}$$

Here $\boldsymbol{U}$ is the instantaneous velocity and can be written as the sum of average velocity and the velocity fluctuations, i.e.

$$\boldsymbol{U} = \overline{\boldsymbol{U}} + \boldsymbol{U}' \tag{3.14}$$

Substituting Eq. (3.14) in Eq. (3.13) and averaging it w.r.t. time, we get

$$\nabla \cdot \overline{\boldsymbol{U}} = 0 \tag{3.15}$$

Now using Eq. (3.13), Eq. (3.14) and Eq. (3.15) we can write

$$\nabla \cdot \boldsymbol{U}' = 0 \qquad \Longrightarrow \frac{\partial u_i'}{\partial x_i} = 0 \tag{3.16}$$

Now substituting the Fourier series of u_i' from Eq. (3.12) into Eq. (3.16), we get a relationship between k_n and σ_n, i.e.

$$k_n \cdot \sigma_n = 0, \quad n = 1, \ldots, N \tag{3.17}$$

This implies the unit direction vector (σ_n) is always perpendicular to wave vector (k_n). Fig. 3.3 below shows the wave vector geometry in relation to the unit vector. The unit direction vector σ_n lies in (k_1', k_2') plane and is at an angle α_n with k_1'. The plane defined by (k_1', k_2') is perpendicular to k_n to satisfy Eq. (3.17). The unit vector σ_n can be expressed in terms of the original coordinate system (k_1, k_2, k_3) and then equating its dot product with the wave vector k_n to 0, gives the value of polar angle α_n Wave vector and the direction vector can be written as:

$$k_n = (\sin\theta_n \cos\phi_n)k_1 + (\sin\theta_n \sin\phi_n)k_2 + (\cos\theta_n)k_3 \tag{3.18}$$

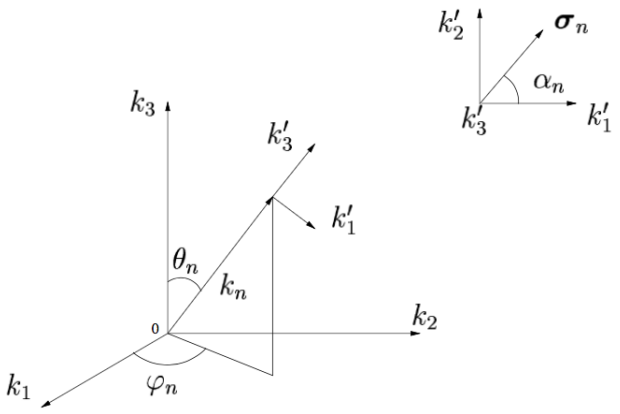

Figure 3.3: k_n and σ_n for n-th Fourier Mode Billson (2004)

$$\sigma_n = k_1' \cos\alpha_n + k_2' \sin\alpha_n \tag{3.19}$$

The original coordinate system (k_1,k_2,k_3) can be transformed into the (k_1',k_2',k_3') system by first rotating it counter-clockwise about k_3 by an angle ϕ and then rotating the resulting system clockwise about k_2 by an angle θ. The resulting transformation can be written in the matrix form as,

$$\begin{bmatrix} k_1' \\ k_2' \\ k_3' \end{bmatrix} = \begin{bmatrix} \cos(\phi_n) & \sin(\phi_n) & 0 \\ -\sin(\phi_n)\cos(\theta_n) & \cos(\phi_n)\cos(\theta_n) & \sin(\theta_n) \\ \sin(\phi_n)\sin(\theta_n) & -\cos(\phi_n)\sin(\theta_n) & \cos(\theta_n) \end{bmatrix} \begin{bmatrix} k_1 \\ k_2 \\ k_3 \end{bmatrix} \tag{3.20}$$

Using the above transformation the unit vector σ_n can be rewritten as,

$$\begin{aligned} \sigma_n &= k_1' \cos\alpha_n + k_2' \sin\alpha_n \\ &= \cos(\alpha_n)\big[\cos(\phi_n)k_1 + \\ &\sin(phi_n)k_2\big] + \sin(\alpha_n)\big[-\cos(\theta_n)\sin(\phi_n)k_1 + \cos(\theta_n)\cos(\phi_n)k_2 + \sin(\theta_n)k_3\big] \\ &= \big[\cos(\alpha_n)\cos(\phi_n) - \cos(\theta_n)\sin(\phi_n)\sin(\alpha_n)\big]k_1 + \\ &\big[\cos(\alpha_n)\sin(\phi_n) + \cos(\theta_n)\cos(\phi_n)\sin(\alpha_n)\big]k_2 + \big[\sin(\alpha_n)\sin(\theta_n)\big]k_3 \end{aligned} \tag{3.21}$$

The polar angle (α_n) can then be calculated by satisfying the condition given in Eq. (3.17) using Eq. (3.18) and (3.21)

$$\alpha_n = \tan^{-1}\Big(-\frac{1}{\cos\theta_n}\Big) \tag{3.22}$$

The isotropy and homogeneity of the random velocity fluctuations is ensured by treating ϕ_n, ψ_n and θ_n as random variables using probability density functions. A random number generator is used to generate a set of random values and these random values are used to calculate ϕ_n, ψ_n and θ_n along with the use of probability density function as given below,

$$P(\phi_n) = \frac{1}{2\pi} \tag{3.23}$$

$$P(\psi_n) = \frac{1}{\pi} \tag{3.24}$$

$$P(\theta_n) = \frac{1}{2}\sin(\theta_n) \tag{3.25}$$

The characteristic angular frequency of the turbulent eddies associated is given by,

$$\omega_n = \epsilon^{1/3} k_n^{2/3} \tag{3.26}$$

Each of the eddies has a certain amount of kinetic energy associated with it depending on the intensity of the velocity fluctuations. The distribution of the turbulent kinetic energy across the eddies is called the energy spectrum. The area under the energy spectrum represents the total kinetic energy of the velocity fluctuations as described earlier in section 3.2.1. The amount of energy contained at each wave number for isotropic turbulence is given by the modified Von Karman spectrum (Hinze, 1975).

$$E(k,t) = 2^{17/6} E(k_e) \frac{(k/k_e)^4}{\left[1 + (k/k_e)^2\right]^{17/6}} \exp[-2\nu\tau_\eta] \tag{3.27}$$

where k_e is the wave number at which $E(k,t)$ reaches its maximum. Hence it is the length scale that contains the maximum energy. τ_η is the Kolmogorov time scale. The value of the maximum kinetic energy $E(k_e)$ is given by

$$E(k_e) = A\frac{2K}{3k_e} \tag{3.28}$$

where A is a constant and K is the total turbulent kinetic energy. The 2 unknowns here are A and k_e and are determined from the following relationships. In the inertial sub-range, the energy spectrum can be described as

$$E(k_n) = A\epsilon^{2/3}(k_n)^{-5/3} \tag{3.29}$$

We can equate Eq. (3.27) ignoring the exponential term (due to negligible viscosity effects) with Eq. (3.29) and using the fact that in inertial sub-range $k/k_e >> 1$, we get the value of k_e,

$$k_e = 2^{-17/4}\left(\frac{3}{2}\right)^{3/2} \frac{\epsilon}{K^{3/2}} \tag{3.30}$$

The turbulent kinetic energy is defined as

$$K = \int_0^\infty E(k)dk \tag{3.31}$$

Substituting Eq. (3.27) and Eq. (3.28) in Eq. (3.31), we can get the value of A

$$A = 3\left[2^{17/6}\int_0^1 \frac{\eta^{3/2}}{(1-\eta)^{2/3}} \exp\Big[-\beta\frac{\eta}{(1-\eta)}(t-t_0)\Big]d\eta\right]^{-1} \tag{3.32}$$

where $\beta = 2\nu k_e^2$. Using the obtained values of A and k_e, the value of kinetic energy for each mode can be calculated using Eq. (3.27). The total turbulent kinetic energy can be written as the summation of energy contained at each eddy scale,

$$K = \int_0^\infty E(k)dk = \frac{1}{2}u_i' u_i' \tag{3.33}$$

Using Eq. (3.12) and Eq. (3.33), the turbulent kinetic energy can be written as,

$$K = \sum_{n=1}^{N} \tilde{u}_n^2 = \int_0^\infty E(k)dk \tag{3.34}$$

The amplitude of the fluctuations ($\tilde{u}_n$) can be calculated by dividing the area under the $E(k)$ vs k curve into a number of smaller rectangles to get

$$\tilde{u}_n = \sqrt{E(k_n)\exp(\Delta k_n)} \tag{3.35}$$

where the continuous distribution of wave numbers is discretized using a logarithmic distribution of N wave numbers. The logarithmic step (Δk_n) is defined as

$$\Delta k_n = \frac{\log(k_N) - \log(k_1)}{N-1} \tag{3.36}$$

with k_1 and k_N being the wave numbers corresponding to the largest eddy and the smallest eddy (Kolmogorov scale) respectively and are given as,

$$\begin{aligned} k_1 &= \frac{2\pi}{L} \\ k_N &= \left(\frac{\epsilon}{\nu^3}\right)^{1/4} \end{aligned} \tag{3.37}$$

The convective velocity of each fluctuation is calculated using ω_n and k_e as follows

$$\bar{u}_c = \frac{\omega_n}{k_e}. \tag{3.38}$$

Using all the above parameters the velocity fluctuations as described in Eq. (3.12) can be calculated.

3.2.3 Calculating the pressure fluctuation field and traction at the fluid-surface interface

The pressure fluctuation field is then computed using the velocity fluctuation field data and the Poisson's equation using Eq. (3.9). In a typical fluid structure interaction solver, the fluid solver takes the displacement from the structural solver as its input and gives the traction as the output as shown in Eq. (2.27). However in this case the pressure fluctuations (p') are added to the mean pressure ($\overline{p}$) which is used in addition to the wall shear stress to calculate the traction at the interface.

$$\text{Pressure Force} = \int (\bar{p} + p')dA \tag{3.39}$$

This ensures that the force exerted on the structure also includes the components due to the pressure fluctuations, which in turn acts as an external excitation condition for the turbulence induced vibrations.

3.3 Numerical Code

The code used for this thesis project is a modified version of Openfoam-Extend project (OpenFOAM). The synthetic fluctuation modeling has been implemented in the FOAM-FSI library to simulate FSI problems. OpenFOAM has been externally coupled to a FEM (Finite Element Method) package Deal.II (Bangerth et al., 2016) using the coupling library preCICE Bungartz et al. (2016). Deal.II is a Finite Element library containing all the required tools to discretize and solve partial differential equations using FEM. Thus it is suited for the structural equation. preCICE (Precice Code Interaction Coupling Environment) is a highly flexible open source coupling library for multi-physics simulations.

3.4 Influence of Using Separate Time Marching Schemes for Fluid and Solid Domain

In a partitioned coupling approach different time marching algorithms can be used in the fluid and the structural domain. To study the influence of different time marching schemes, a simplified 1-D piston problem (Piperno et al., 1995) is used as a test case. All the possible combinations of the time marching schemes available in the individual fluid (OpenFOAM) and the structural (Deal.II) solver are studied. Based on this study Backward Differencing Formula-2 for the fluid solver and Crank-Nicolson for the structural solver is chosen as the time marching scheme combination that is used in all the further simulations. The details of this analysis have been shown in Appendix A.

3.5 Summary

This chapter gives a brief overview of different approaches to studying turbulence in a flow field. The procedure of applying averaging methods to separate the mean and fluctuating components of variables using Reynolds Averaged Navier-Stokes methods is described in a bit more detail. However using U-RANS models for studying turbulence induced vibrations has a major drawback that the amplitude of the oscillation cannot be predicted due to the damping out of instantaneous fluctuations in the flow field. Senthooran (2002) identified a way to model the turbulent velocity fluctuations in a flow field as a discrete Fourier series using known parameters such as the turbulent kinetic energy and its dissipation rate from the U-RANS models. An overview of this model is presented in detail. However, the use of this model in Turbulence Induced Vibrations is still only verified qualitatively (Kottapalli, 2016). A quantitative verification of this procedure would require comparing the results of this model with an actual experiment where Turbulence Induced Vibrations are a major source of excitation. However, initially a numerical and experimental validation study for the FSI solver obtained using the preCICE coupling library is performed as described in the next chapter.

Chapter 4

Validation of preCICE Coupling

In this chapter the developed FSI solver is validated against two reference test cases. The first reference test case is the numerical benchmark provided by Turek and Hron (2006). This involves an elastic flap attached to a solid cylinder, both of which are submerged in a channel flow leading to oscillations of the flap. The second test case is an experiment performed by Vattenfall Research and Development, where a slender tube (submerged in water or air) is given an initial displacement at its center and then released to study its damping characteristics (Lillberg, 2015). Both these cases are chosen to quantitatively confirm the implementation of the coupling adapter for the solver described in the previous chapter.

4.1 Numerical Benchmark

A numerical benchmark by Turek and Hron (2006) is used for evaluating the performance of the coupling tool preCICE, which was used to couple OpenFOAM and Deal.II as described in previous chapter. The test case involves a laminar incompressible channel flow encompassing an elastic flap attached to a solid cylinder. The benchmark overall comprises on 9 test cases. The first three test cases viz. CFD1, CFD2 and CFD3 focus only on the fluid dynamics of the domain. Out of the above cases, the flowfield in CFD3 shows oscillations and is chosen to be performed as a test case. The structure only test cases of the benchmark are named CSM1, CSM2 and CSM3. Out of these only CSM3 is time dependent whereas the other two have steady state solutions. Hence CSM3 is chosen to be performed in this study. The final three test cases (FSI1-3) in the benchmark deal with fully coupled fluid structure interaction. FSI1 leads to steady state a steady state deformation whereas FSI2 and FSI3 result in self-sustaining oscillations of the flap. For this study FSI3 is chosen as the validation test case as it is a strongly coupled case with density ratio of the fluid and the solid being one.

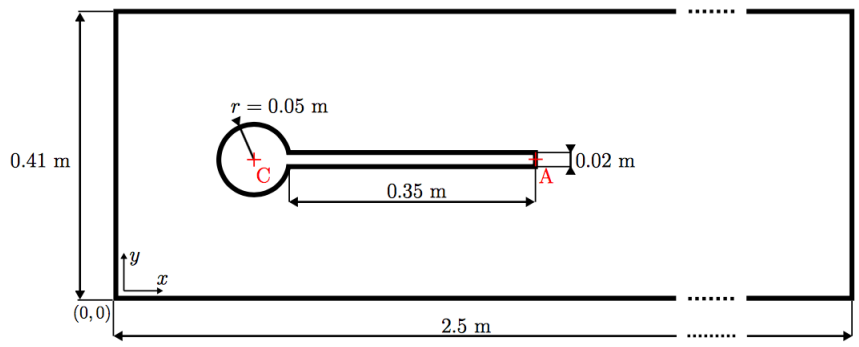

Figure 4.1: Computational domain showing the fluid and the structural domain (Gatzhammer, 2014)

4.1.1 Domain Description

The domain comprises of a 2-D flap attached on the rear end of a cylinder immersed in a channel flow as described in Fig.4.1. The dimensions and coordinates of the domain have been described below:

- The length and width of the channel are 2.5 and 0.41 respectively
- The cylinder is centered at C (0.2,0.2) with a radius of 0.05
- The length and width of the flap are 0.35 and 0.02 respectively.
- Point A refers to the point at which the displacement of the flap is compared.

4.1.2 Boundary Conditions

- A parabolic velocity profile has been initially prescribed at the left wall of the domain as described below,

$$v^f(t,y) = \begin{cases} 1.5\bar{U}\frac{y(H-y)}{\frac{H}{2}^2}\left(\frac{1-cos(\frac{\pi}{2}t)}{2}\right), & \text{if } t \leq 2 \\ 1.5\bar{U}\frac{y(H-y)}{\frac{H}{2}^2}, & \text{otherwise} \end{cases}$$

  where H is the height of the channel i.e. 0.41 and the mean inflow velocity is $\bar{U}$ and the maximum inflow velocity is $1.5\bar{U}$. The outflow condition for the velocity is prescribed as a zero gradient at the outlet.

- The inflow condition for pressure is prescribed as zero gradient at the inlet with some reference value (0 in this case) prescribed at the outlet.

Table 4.1: Physical parameters for test cases performed

Parameter	CFD3	CSM3	FSI3
ρ_f (kg/m^3)	1e3	-	1e3
ν_f (m^2/s)	1e-3	-	1e-3
$\overline{U}$ (m/s)	2	-	2
ρ_s (kg/m^3)	-	1e3	1e3
E^s (kg/ms^2)	-	1.4e6	5.6e6
ν^s	-	0.4	0.4
g (m/s^2)	0	2	0
$\frac{\rho_s}{\rho_f}$	-	-	1

- A no-slip condition has been prescribed at the bottom and top wall of the domain as well as at the walls bounding the structural domain.

4.1.3 Physical Properties and Simulation Setup

The physical properties for all the test cases performed have been shown in table 4.1.

The coupled Fluid Structure Interaction case is performed using three increasingly refined grids both for the fluid and the structure domain named coarse, fine-1 and fine-2. The number of cells in the fluid domain for each of the above grids is 5981, 23924 and 92984 respectively. The structural grid is refined in accordance with the fluid grid to keep the cells at the fluid structure interface conformal. All 3 grades of the fluid mesh have been shown below in Fig. 4.2, 4.3 and 4.4.

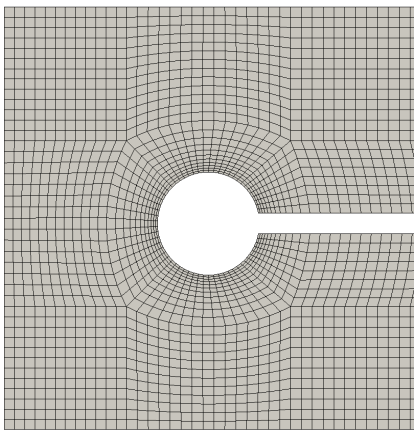

Figure 4.2: Mesh-coarse

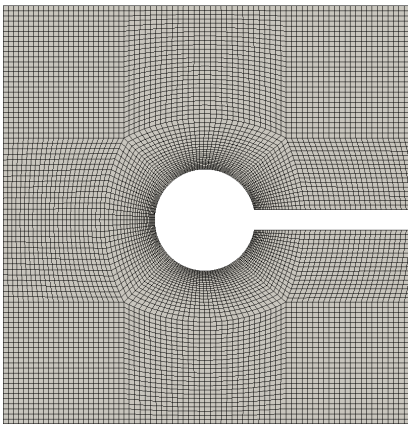

Figure 4.3: Mesh-fine1

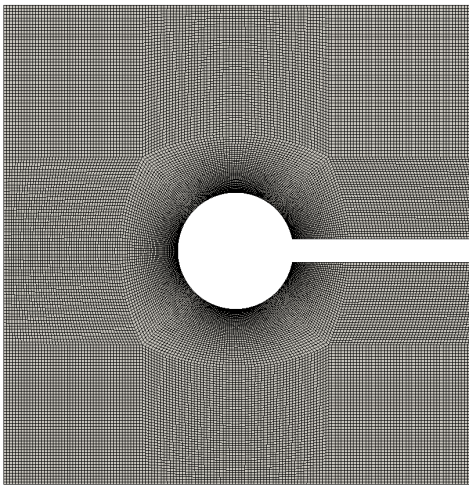

Figure 4.4: Mesh-fine2

4.1.4 Results and Discussions

This section provides the comparison of the simulations for the CSM3, CFD3 and FSI3 cases with the data provided for these by Turek and Hron (2006). The first section compares the y-displacement of the point-A on the beam for the transient structure only simulation. The second section provides the results obtained for the fluid only transient simulation CFD3 and compares the lift and drag acting on the structure with data provided in the reference case. Finally the last section compares the y-displacement history for a transient Fluid-Structure Interaction case FSI3 with the reference data.

4.1.4.1 Hron and Turek CSM3

The CSM3 test case shows the response of point A on the flap oscillating under the influence of gravitational force of 2 m/s^2 without being submerged in fluid. The time integration method used is Crank-Nicolson. Fig. 4.5 shows the displacement history of point-A for 3 grades of structural mesh consisting of 254, 500 and 1325 elements respectively. A time step (Δt) of 0.001s was chosen for this simulation. The properties of the solid are mentioned in the second column of table 4.1. It can be observed that the magnitude of displacement is in practically indistinguishable at first but is slightly damped after a few oscillation cycles. The maximum measured deviation in amplitude is 3% from the reference data. Also the frequency of oscillation is slightly underpredicted in this simulation. The overall results are in good agreement with the reference data. The slight variation might be due to the use of linear elasticity model for the structural solver. Another source of uncertainty is how the 2-D flap is attached to the cylinder. Based on the dimensions described in Section 4.1.1 a gap (δl) would be created at the intersection of the cylinder and beam as shown in Fig. 4.6. It is not clear whether this gap is intended or not.

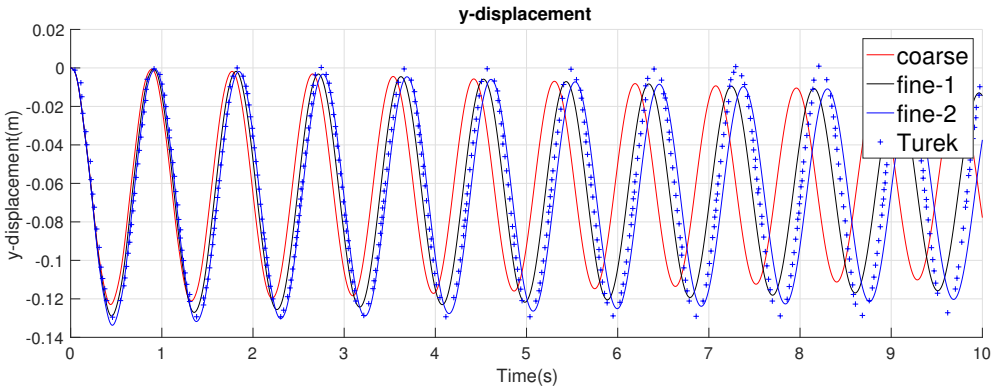

Figure 4.5: y-displacement of point-A (CSM3)

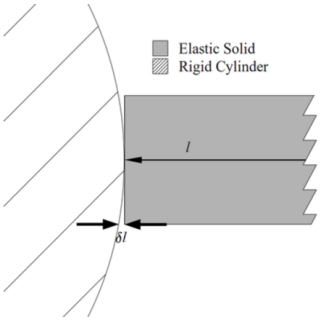

Figure 4.6: Close-up of the gap between cylindical and beam section of the structure (Sheldon, 2012)

4.1.4.2 Hron and Turek CFD3

This test case is focused on the fluid dynamics part of the problem. The fluid only simulation is performed by making the structural beam almost rigid using large values for the structural parameters (ρ_S and E^s are of the order 10^6 and 10^{12} respectively). This simulation is performed on the finest fluid grid i.e. fine2 using BDF2 as the time integration method with Δt= 0.001s. The lift and drag forces on the structure are calculating by adding up the forces along the cylindrical part and the beam of the structural domain. A snapshot of the velocity and pressure contours at t = 5s has been shown in Fig. 4.7 and Fig. 4.8 respectively. The unsteadiness of the flow can be clearly observed from the velocity profile. The quantitative analysis is performed using the the lift and drag forces acting on the structure. It can be observed from Fig. 4.9 that the computed lift forces are practically indistinguishable from the reference data. The drag forces have been shown in Fig. 4.10 and the maximum deviation from the reference data for these is 0.2%. Hence it can be concluded that the fluid only simulations are in good agreement with the reference data. Also, a slight variation in frequency of oscillation for both the lift and drag forces piles up with time and can lead to a phase shift,

hence to make the comparison between the performed simulation and the reference data from t = 9s to t = 9.6s, this phase shift has been removed.

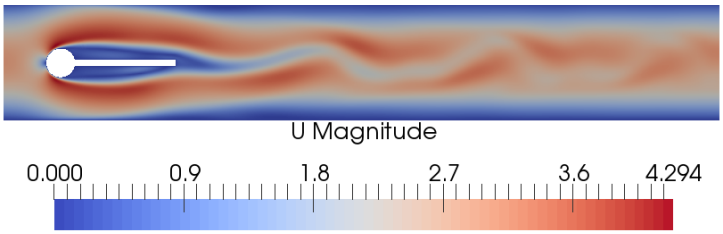

Figure 4.7: Velocity contours at t = 5s [m/s] (CFD3)

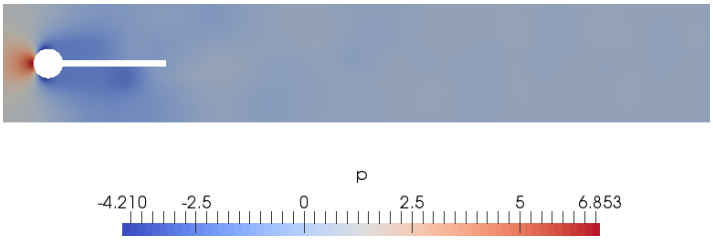

Figure 4.8: Pressure contours at t = 5s [Pa] (CFD3)

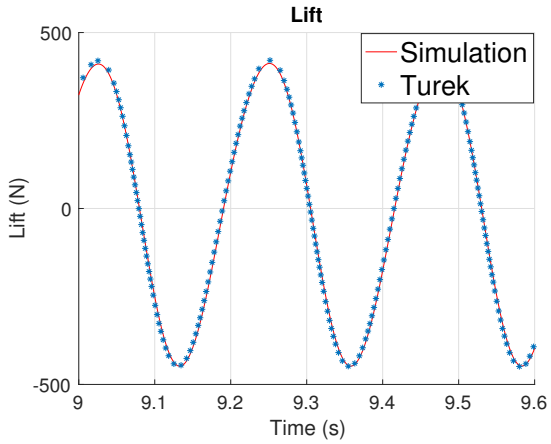

Figure 4.9: Lift force on the cylinder + beam (CFD3)

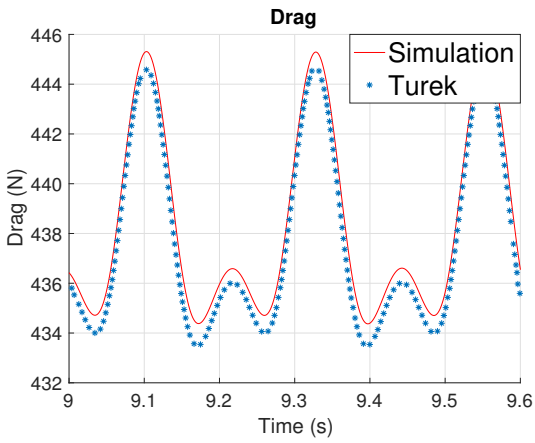

Figure 4.10: Drag force on the cylinder + beam (CFD3)

4.1.4.3 Hron and Turek FSI3

This is the final numerical test case meant to evaluate the capabilities of the fluid structure interaction solver. This test case comprises of the same geometry as before i.e. a slightly off-center cylinder with a beam attached to it, both of which are submerged in a channel flow

domain as shown in Fig. 4.1. The time integration method used for the fluid and the structural solver is BDF2 and Crank-Nicolson respectively. The coupling algorithm used between the two domains is IQN-ILS, the mesh motion is computed using Radial Basis functions (Thin Plate Spline) and the data interpolation method used is Nearest Neighbor Projection as the mesh used for this case is conformal.

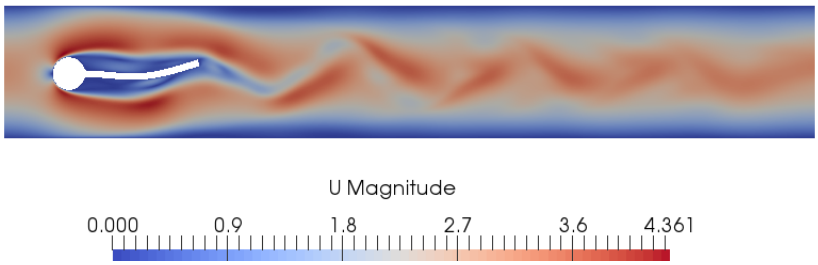

Figure 4.11: Velocity contours at t = 10s (in m/s)

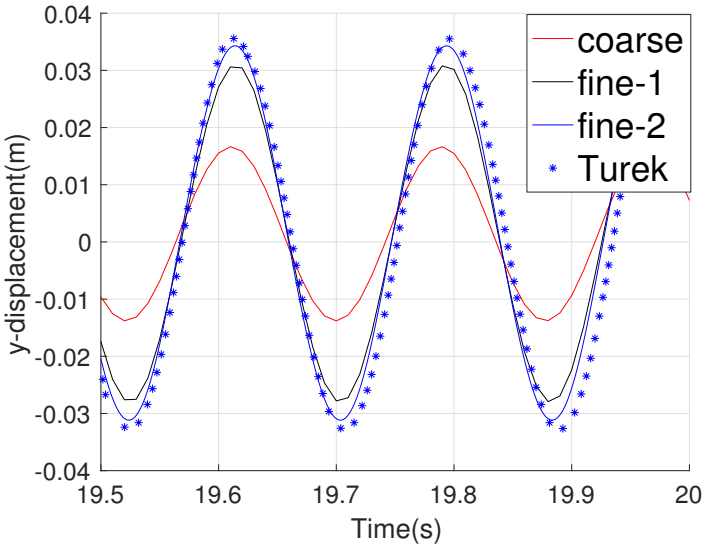

Figure 4.12: y-displacement of point A (FSI3)

A snapshot of the velocity contour at t= 10s is shown in Fig. 4.11 which highlights the unsteadiness of the flow. A quantitative comparison with the reference data is done by plotting the y-displacement of point-A on the beam for all 3 grades of the mesh and the reference data. It can be observed that the computed displacement gets increasingly closer to the reference data with finer grids. The computed displacement for the fine-2 grid is in good agreement with reference data; the maximum error in displacement being 3%. The comparison of the mean and the amplitude of the y-displacement history is shown in Table 4.2. Similar to the Hron and Turek CFD3 case, the phase shift has been removed for this case too. The decreased amplitude compared in Fig. 4.12 can be attributed to the artificial damping introduced by the temporal and spatial discretization. Similar to the phase shift,

the damping of amplitude also adds up with time.

Table 4.2: Mean and amplitude of the y-displacement of point A for FSI3

Case	**y-displacement Mean** (m)	**y-displacement Amplitude** (m)
Coarse	0.0021	0.0146
Fine 1	0.0020	0.0289
Fine 2	0.0013	0.0330
Turek	0.0016	0.0340

In this section the most relevant test cases from Turek and Hron (2006) were selected viz. CSM3, CFD3 and FSI3; and were performed using the developed Fluid Structure Interaction solver and a good agreement with the reference results for all three cases was observed.

4.2 Experimental Benchmark

Vattenfall Research and Development in Sweden performed an experiment (Lillberg, 2015) tailored to be a validation case for fluid structure interaction codes especially for nuclear reactor applications. The test case involved a vertical beam completely immersed in water which is clamped at the fluid inlet side and has a roller boundary condition at the fluid outlet. The center of this beam is given an initial displacement of 10mm and then released to study its vibrations and damping characteristics both in air and water.

4.2.1 Experimental Setup

The experimental setup consists of a slender stainless steel beam of length 1.5m contained inside a plexiglass channel of the same length with a cross section of 0.8m $\times$ 0.8m. The cross section of the beam is 8cm $\times$ 20cm. The beam is clamped at the fluid inlet side of the domain whereas it has 'roller type' support on the other end. This roller type support allows the beam to move in the axial direction while restricting its motion in the other two normal directions. Construction drawing of beam is shown in Fig. 4.13.

The flow of the water is maintained using pumps in the beam longitudinal direction. To impose the displacement on the beam, a fine line is attached to the bar, which is then pulled back until the beam displaces by 10mm and is finally cut to initiate the experiment. The step by step schematic of this procedure is shown in Fig. 4.14. The displacement history of the beam is then measured using a laser.

The measurements were made initially for quiescent air and water and subsequently with varying axial inlet velocities of water through the channel. The stainless steel beam used has a density (ρ) = 8000 kg/m^3 and a modulus of elasticity (E) equal to 188 GPa. The two tests used for reference purposes for this study are: with quiescent air at a temperature of 17.7° C

and with water flow of 1m/s at a temperature of 8.4° C.

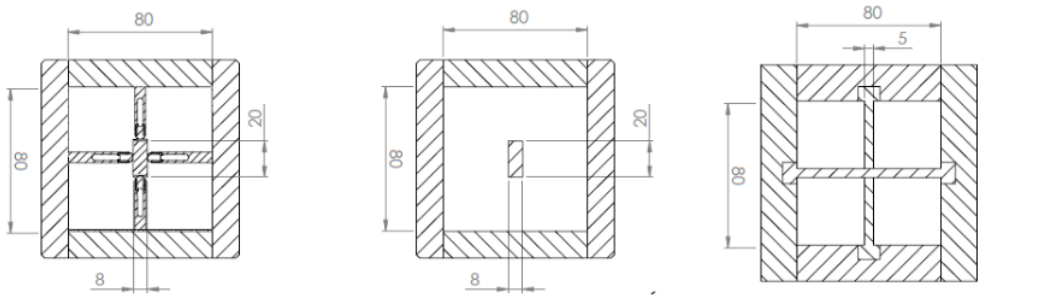

(a) Top of rod, 'roller' boundary condition

(b) Rod at half length, free

(c) Bottom of rod, clamped boundary condition

Figure 4.13: Boundary conditions of the steel beam at different locations

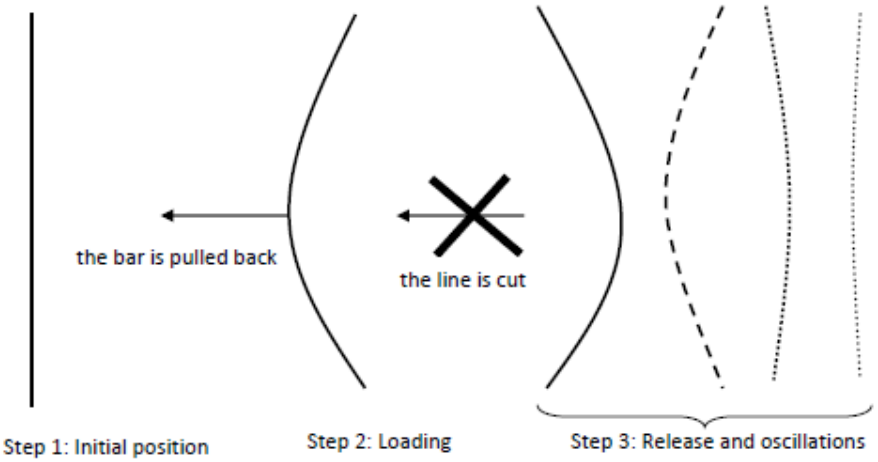

Figure 4.14: Schematic of steps involved in displacing the beam

4.2.2 Computational Domain

A schematic and the dimensions of the computational domain is shown in Fig. 4.15, where L = 1.5m, H = 0.8m, a = 0.75m, h = 8mm, l = 20mm and δ = 10mm.

The difficulty in replicating the 'roller' boundary condition and the effect of number of axial elements in the solid mesh on predicting the oscillation frequency of the beam was reported by Ter Hofstede (2015). Hence a solid only simulation is performed initially to assess the efficacy of the structural solver in Deal.II in being able to capture the dynamics of the experiment.

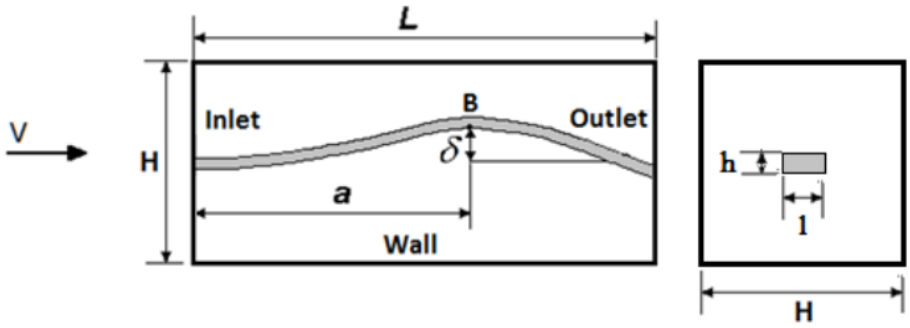

Figure 4.15: Dimensions of the Vattenfall computational domain

4.2.3 Structure Only Simulation

Five grades of structural mesh have been used for this study, each with 80, 160, 320, 640 and 1280 axial elements respectively. The cross-section of the beam has 8 × 4 elements for all these cases. The structural mesh for each of these cases has a small patch of length 0.02m at the exact center of the beam. This patch is provided an initial displacement of 10mm and then released to study the damping characteristics of the beam. All these simulations have been performed using both Backward Euler and Crank-Nicolson time integration schemes with a time step size of $\Delta t = 0.001$s. The reference data for this study is from the first experiment performed by Lillberg (2015), where the displacement of the beam is measured in quiescent air. The experimental frequency of vibration was observed to be 12.3 Hz. The analytical frequency for a fixed-roller type supported beam can be calculated using Rajasekaran (2009)

$$\omega = \frac{1}{2\pi} \frac{15.418}{L^2} \sqrt{\frac{EI}{\rho A}}, \tag{4.1}$$

where L, E, I, ρ, A are the length of the beam, the modulus of elasticity, the moment of inertia, the density of the beam and the cross-section area respectively. The computed analytical frequency for the current beam geometry is 12.37 Hz, which is very close to the experimentally measured frequency. The simulation results for 0.1s of oscillation after being initially displaced by 10mm are shown in Fig. 4.16. The results for specifically the structural mesh with 640 and 1280 axial elements has been shown separately in Fig. 4.17 to make it more readable and compare it with the experimental data. A clear trend of better approximation of the experimental frequency with increasing axial elements is observed from both the figures. It can also be observed that the Crank-Nicolson time integration scheme better approximates the amplitude of the oscillations whereas Backward Euler introduces artificial damping, thus reducing the amplitude of oscillation. A quantitative comparison of the frequency of oscillation for each of the cases has been provided in table 4.3.

From this section it can be concluded that the structural solver implemented in Deal.II is

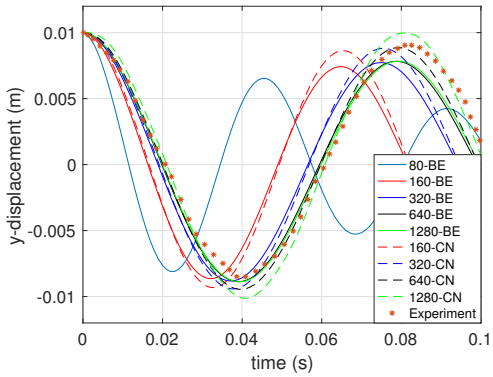

Figure 4.16: Displacement history for simulations with varying number of axial elements (BE and CN represent Backward Euler Crank-Nicolson time integration schemes respectively)

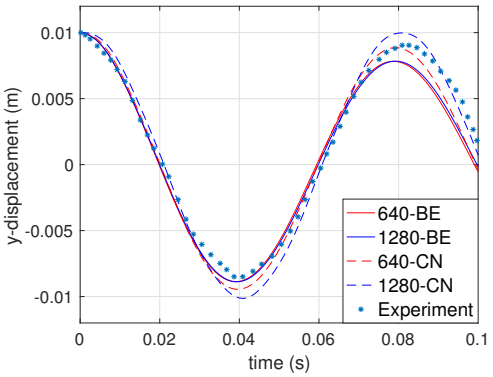

Figure 4.17: Displacement history for simulations with 640 and 1280 axial elements

Table 4.3: Frequency of oscillation for each of the simulated cases (BE and CN represent Backward Euler and Crank-Nicolson time integration schemes respectively)

Case	**Frequency** (Hz)	**Error** (%)
Experiment	12.3	-
80-BE	21.739	76
160-BE	15.150	23
320-BE	13.158	6.9
640-BE	12.821	4.2
1280-BE	12.658	2
160-CN	15.385	25
320-CN	13.333	8.3
640-CN	13.158	6.9
1280-CN	12.500	1.62

capable of replicating the dynamics of the experiment especially the 'roller' type boundary condition. Based on the simulation results it is decided that the number of axial elements for the Fluid Structure Interaction study will be 640.

4.2.4 Coupled Fluid Structure Interaction

This sections deals with the simulation performed to replicate the second experiment carried out at Vattenfall Research and Development Lillberg (2015). This experiment involves studying the damping characteristics of the steel beam (initially displaced by 10mm) surrounded by a water flow of 1m/s through the plexiglass channel. Two different grades of fluid mesh are chosen for this study to establish that the structural damping characteristics are independent

of the fluid mesh element size. The coarse and the fine fluid mesh consist of 51200 and 409600 elements respectively and the structural mesh has 20480 cells with 640 axial elements. Different cross-sectional views of the fluid and structure mesh have been shown in Fig. 4.18. The time marching algorithm used in these simulations is Crank-Nicolson for the structure while BDF-2 is used for the fluid with a time step size (Δt) of 0.001s. Both the fluid and structural domain are being solved throughout the simulation, but the transfer of traction was stopped while the structural beam was being initially displaced by 10mm. Once the beam had been displaced by 10mm, all the constraints on the central patch of the structure (which is used to displace the beam) were removed and the beam was free to oscillate bound at the 2 ends with clamped and roller type boundary conditions.

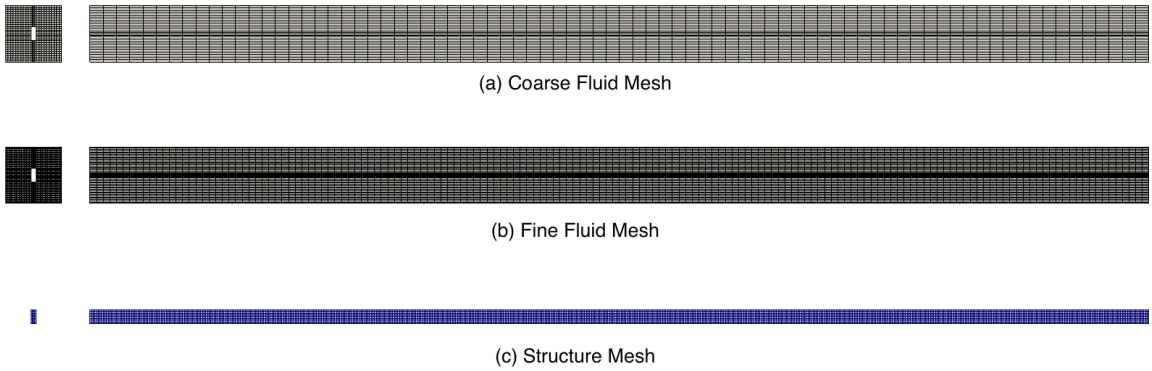

Figure 4.18: Fluid (black) and structure (blue) mesh used for the FSI simulation

The boundary conditions imposed on the fluid domain have been listed in table 4.4. The flow inlet velocity has been imposed at the inlet with a zero gradient at the outlet. At the outer walls of the fluid domain a no-slip boundary condition has been imposed, whereas on the inner walls i.e. the fluid structure interface a no slip boundary condition would imply the fluid velocity being equated to the velocity of the structure at the interface. For the pressure field a zero gradient has been imposed at all the boundaries except at the outlet where a fixed value of 0 has been imposed. The discretization setting for the the gradients, laplacian and divergence terms for the fluid solver along with the time marching algorithm have been shown in table 4.5.

Table 4.4: Boundary conditions for the flow variables in OpenFOAM

Variable	Inlet	Outlet	FSI-interface	Outer Walls	Units
U	(0,0,1)	zero gradient	structural velocity	no slip	ms^{-1}
p	zero gradient	0	zero gradient	zero gradient	m^2s^{-2}

Table 4.5: Settings for the solver

	Scheme
ddtSchemes	bdf2
ddtSchemes (Structure)	Crank-Nicolson
gradSchemes	Gauss linear
divSchemes	Gauss linearUpwind
laplacianSchemes	Gauss linear corrected
snGradSchemes	corrected
Mesh motion	Radial Basis Functions (Thine plate spline)
Coupling Algorithm	IQN-ILS
Maximum coupling iterations	60

4.2.4.1 Fluid Grid Independence

Fig. 4.19 shows the response of the structure after being displaced by 10mm for both the grades of the fluid mesh shown in Fig. 4.18 and for structural mesh with 640 axial elements as was motivated in section 4.2.3. It can be clearly observed that increasing the fluid grid resolution by 8 fold does not lead to any significant changes in response of the structure, hence the grid independence can be established for the fluid domain too. For the rest of the chapter the coarse mesh is thus used to save computational costs.

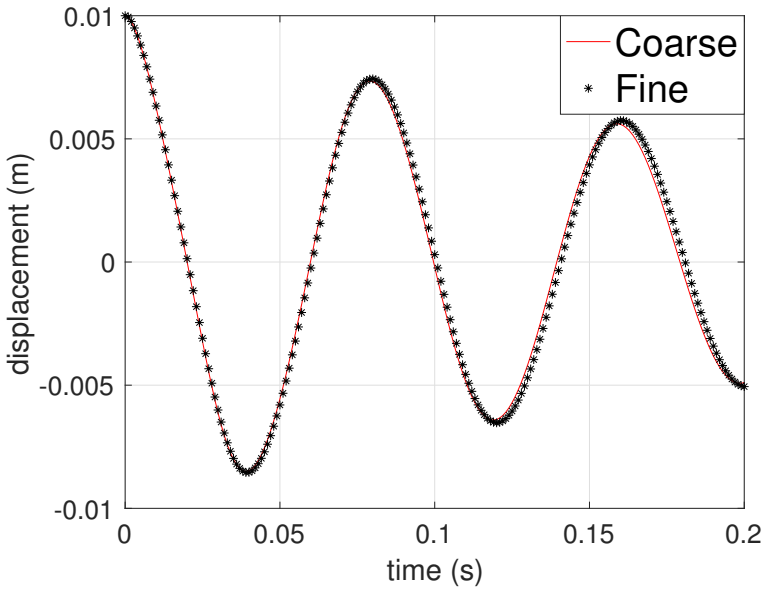

Figure 4.19: Displacement history of the center of the beam with varying grades on fluid mesh

4.2.4.2 Results and Discussion

Fig. 4.20 shows the displacement of the center of the beam for the complete simulation runtime. For the first 0.5 seconds of the simulation, the center of the beam is displaced by 10mm using the following relation for the displacement,

$$y = 0.5(y_i)\Big[1 - cos\Big(\frac{t}{t_{\text{ramp}}}\Big)\Big] \tag{4.2}$$

where y is the displacement of the beam, y_i is the final displacement to be imposed i.e. 10mm in this case, t_{ramp} is the time taken to impose the given displacement and t is the time at which the displacement is being evaluated. This specific relation is chosen so as make sure that the beam does not have any velocity at the end of the time taken to impose a displacement. After the displacement has been imposed on the beam i.e. after 0.5 s, the traction is turned on for the coupled fluid structure interaction case which is from 0.6s to 0.7s and is shown separately in Fig. 4.21. The frequency of oscillation of the beam is noted to be 10Hz for the experiment, whereas the frequency of oscillation for the simulation was calculated to be 9.901 Hz. Hence the results of this simulation are in good agreement with the experiment with a 0.99% error in the oscillation frequency.

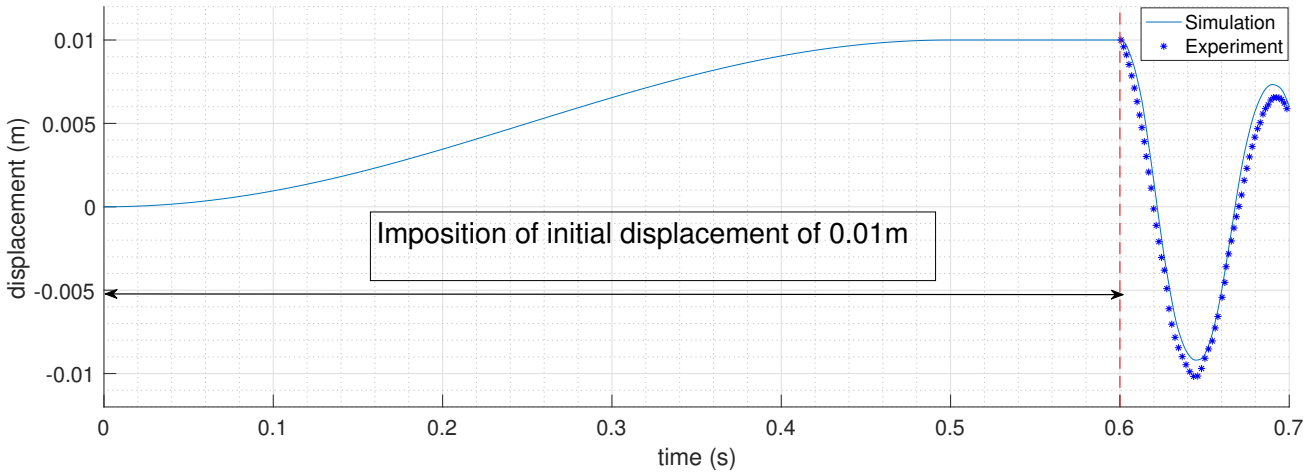

Figure 4.20: Displacement history of the center of the beam for simulation with water flow of 1m/s

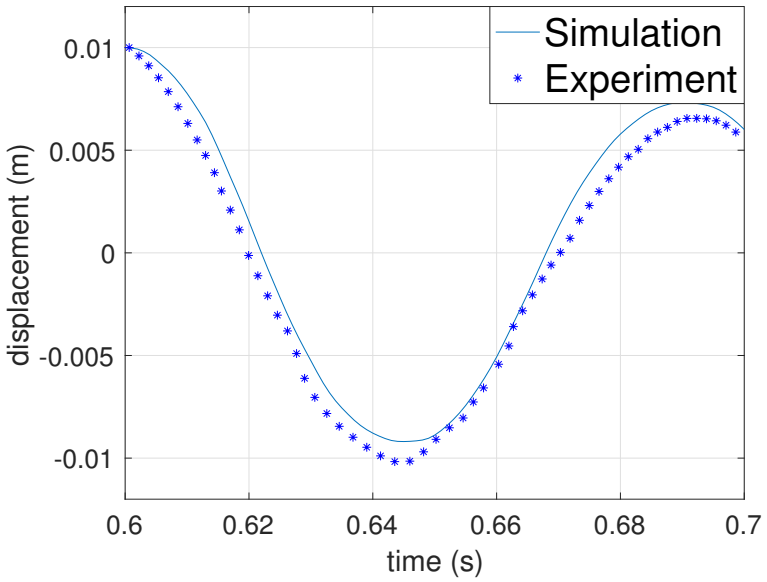

Figure 4.21: Displacement history of the center of the beam during coupled fluid and structure simulation

4.3 Summary

Two different validation studies were performed in this chapter. The first one was a numerical benchmark for Fluid Structure Interaction solvers by Turek and Hron (2006). Three test cases each for all 3 aspects of the Fluid Structure Interaction solver i.e. the fluid dynamics, structural mechanics and the coupled interaction were chosen from this benchmark viz. CFD3, CSM3 and FSI3. It was observed that the developed solver provides simulation results that are in good agreement with the reference data. Also the coupled FSI case chosen was a strongly coupled problem, thus validating the efficacy of this solver in handling strongly coupled cases which are usually observed in nuclear reactors. The second validation case used was an experiment conducted at the Vattenfall Research and Development Lillberg (2015) involving a 3-D steel beam immersed in quiescent air and a water flow channel. In this case initially the capability of the structural solver to replicate the 'roller' boundary condition was first validated and then a coupled FSI simulation of steel beam in channel flow of water was performed. The results obtained were again in good agreement (0.99% error in frequency) with the experiment.

Chapter 5

Validation of Synthetic Turbulent Fluctuations for TIV

This chapter presents two test cases that are used to validate the use of synthetic turbulent fluctuation modeling in order to simulate turbulence induced vibrations. The first test case is a variation of the geometry used by Turek and Hron (2006). In this case the cylindrical portion in front of the Turek geometry is removed in order to remove the excitation of the flap due to vortex shedding. The second test case in an experiment performed by Liu et al. in which a steel cylinder fixed at one end and free at the other end is subjected to axial water flow from the direction of the free end. The oscillation frequency and the amplitude of vibrations is available from this test case to quantitatively validate the efficacy of synthetic fluctuation modeling.

5.1 Steel flap fixed on both ends

In this test case, a steel flap is fixed at both ends and submerged in a turbulent water flow. The fluid and the steel flap mesh along with the domain are shown in Fig. 5.1. The inlet flow velocity is 10 m/s. The outlet is a fixed pressure boundary condition with both the upper and the lower boundaries as walls with no slip boundary condition. Both, the left and the right end of the flap are given a Dirichlet boundary condition with zero displacement. The bulk Reynolds number of the flow is 4×10^6 using the inlet height as the reference length. The fluid mesh has 102 $\times$ 43 quadrilateral elements. The solid domain has 200 quadrilateral elements. The time marching scheme used is BDF-2 for the fluid domain and Crank-Nicolson for the structural domain with a step size of 0.001s. Since the Reynolds number is of the order 10^6, the water flow is reasonably turbulent. Due to this turbulence the pressure fluctuations in the water are sufficient to externally excite the steel flap. To study the influence of synthetic fluctuation modeling, two variations of this test case are performed. The first involves using standard U-RANS model (k-ω with wall functions) and the second involves imposition of

synthetic fluctuation modeling on top of standard U-RANS model.

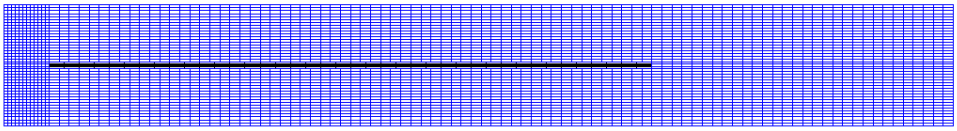

Figure 5.1: Mesh and domain of the Steel Flap in Turbulent Water test case. The length of the fluid domain (in blue) $L = 3.15\ m$, height of the fluid domain $H = 400\ mm$, length of the flap (in black) $l = 2\ m$ and the width of the flap $h = 20\ mm$.

Fig. 5.2 shows the vertical displacement of the center point of the flap. It can be observed from this figure that the synthetic fluctuation modeling is capable of maintaining the vibrations whereas in case of standard U-RANS model the vibrations are damped considerably, hence the amplitude of the vibrations is under predicted as is clear from the r.m.s. values of the displacement shown in Table 5.1.

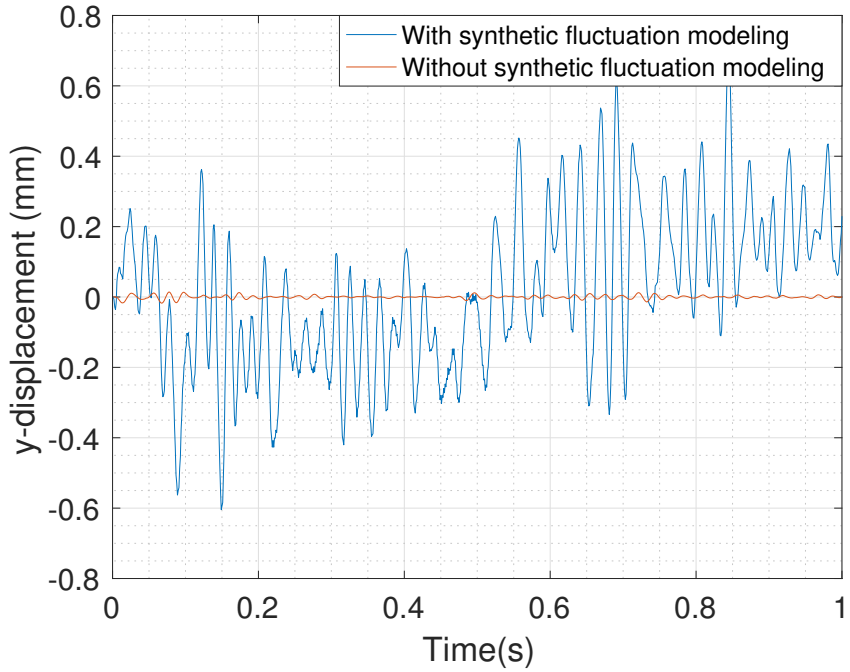

Figure 5.2: Comparison of the structural displacement of the beam center with and without the synthetic turbulent fluctuations

Despite the fact that the model successfully simulates the expected response of the structure, it still needs to be validated against an experimental test case to quantitatively verify if the amplitude response generated by synthetic turbulent fluctuations is physical. The next section deals with the aforementioned requirement.

Table 5.1: Comparison of r.m.s values of the displacement of the flap

Case	**RMS Amplitude** $[\times 10^{-4}\ m]$
Standard $k-\omega$	0.0448
With synthetic fluctuation modeling	2.233

5.2 3-D Cantilever Rod in Axial Water Flow

This test case involves simulating a stainless steel rod submerged in axial water flow. The following subsections describe the experimental setup, the final configuration chosen to be performed numerically, the computational setup of the simulations and finally the comparison of the results with the experimental data.

5.2.1 Experiment Description

Liu et al. experimentally studied a fluid structure interaction system closely related to those found in nuclear reactors cores. The experimental system consists of a hollow cylindrical stainless steel (316L) rod which is free at one end and fixed at the other, mounted inside a coaxial Plexiglas tube. The inner and outer diameter of the cylindrical rod is 8.8 mm and 10 mm respectively and its length is 1.05 m. The Plexiglas tube is 2.05 m long and has an inner and outer diameter of 21 mm and 25 mm respectively. The schematic of the test facility is shown in Fig. 5.3. Through the annulus formed in between the Plexiglas and the cylindrical rod, turbulent water is flow is directed from the bottom end of the test facility towards the top end. Hence the water flow is directed from the free end of the cantilever rod towards the fixed end. Two configurations of the rod free end have been used for this experiment, one with a blunt end and the other with a tapered end as shown in Fig. 5.4. The displacement history of the rod is measured by putting two axially aligned ink marks at a distance of 25 mm from the rod free end and then using fast imaging cameras to track their movement. The obtained displacement history is then used to quantify the vibrations, e.g. the vibrating frequency can be obtained using a Fast Fourier Transform and other parameters such as the maximum and the RMS amplitude values.

5.2.2 Structure Only Simulation

As was observed in Section 4.2.3, the oscillation frequency of a structure is dependent on the number of axial elements in the computational mesh. A certain minimum number of axial elements are required to accurately capture the experimental oscillation frequency. For this purpose a structure only simulation was initially performed to determine a suitable structural mesh for the FSI computation. Liu et al. performed a preliminary test to compare the oscillation frequency of the hollow cylindrical steel rod (described earlier) with the theoretical results. The experiment involved striking the steel rod with a hammer to initialize the vibration and then studying the damping characteristics. The surrounding fluid in this case is

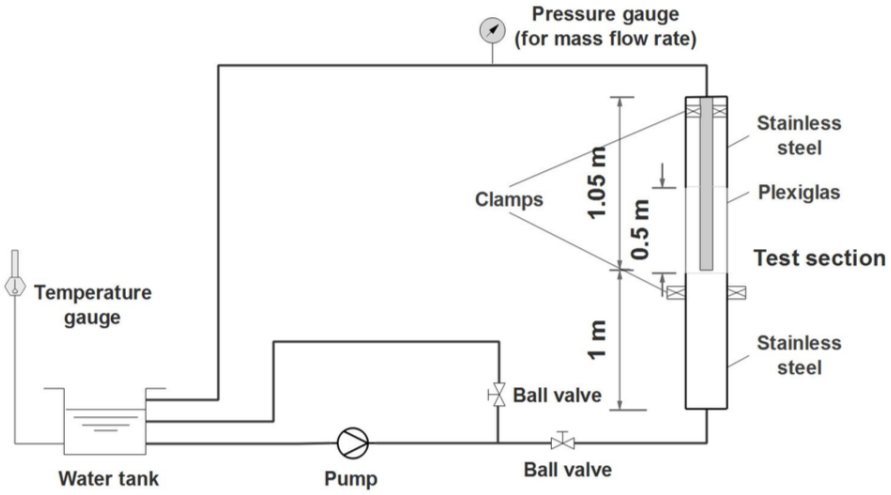

Figure 5.3: Schematic of the test facility (Liu et al.)

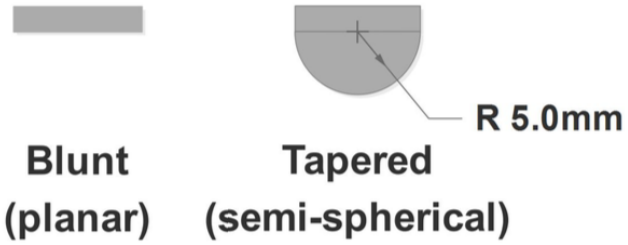

Figure 5.4: Variations of the rod free end (Liu et al.)

air. The displacement history of a point 25 mm axially away from the free end of the steel rod was then recorded. Finally a Fast-Fourier transform was performed on the time history of the displacement to compute the vibration frequency.

The aforementioned experiment was performed numerically for 4 different grades of structural mesh with 42, 105, 210 and 420 axial elements respectively. The cross section of each of these meshes had 40 elements. To replicate the conditions of the experiment the free end of the steel rod is initially displaced by 2 mm and then released to study its damping characteristics. The displacement history of a point 25 mm axially away from the free end of the rod was recorded for each of the geometries. Fig. 5.5 shows the Fast Fourier Transform for each of the displacement histories. The peak of every FFT curve corresponds to the dominant frequency of oscillation for different grades of the mesh. The oscillation frequency for each of the structural mesh used in listed in Table 5.2. The error in the computed frequency is calculated using the experimental frequency as the reference which is 8.3 Hz. Based on these results the number of axial elements for the structural mesh is chosen as 210 for the coupled Fluid Structure Interaction case described in the next section.

Table 5.2: Oscillation frequency for different grades of structural mesh

Number of axial elements	Frequency of oscillation	Error (%)
42	9.4374	+ 13.7
105	8.5453	+ 2.96
210	8.3033	+ 0.04
420	8.2937	- 0.07

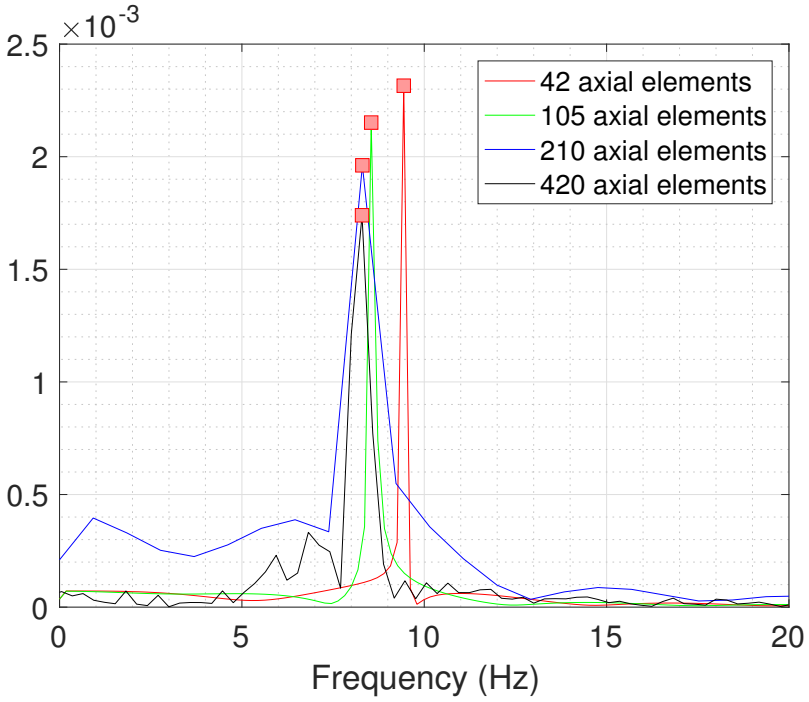

Figure 5.5: Fast Fourier Transform of the displacement histories for different grades of structural mesh (red squares show the dominant frequency)

5.2.3 Coupled FSI Simulation

The experimental case with an inlet flow velocity of 1.49m/s has been chosen as the validation case for the purpose of this thesis. This corresponds to a Reynolds number of 18,342 based on the hydraulic diameter of the annulus. The properties of the fluid and the structure are listed in Table 5.3. Different cross sectional views of the fluid and the structural mesh are shown in Fig. 5.6. The fluid mesh consists of 108170 cells while the structural mesh consists of 8080 cells. The structural mesh contains 210 axial elements based on the structure only simulation study as described in the previous section. The time discretization scheme used for the structural code in Crank-Nicolson while the BDF-2 is used for the fluid domain with a time step size (Δt) = 0.0005 s. The coupling algorithm used is IQN-ILS with 6 time steps being re-used in the algorithm.

The flow inlet velocity of 1.49 m/s has been imposed at the fluid inlet boundary with a

Table 5.3: Material properties used in 3-D cantilever rod case

Fluid Properties (Water at 25°)	
Density (ρ_f)	997.13 kg/m^3
Kinematic Viscosity (ν_f)	8.9×10^{-7} m^2/s
Structural Properties (Steel-316L)	
Density (ρ_s)	8000 kg/m^3
Elasticity Modulus (E)	193 GPa
Poisson Ratio (ν)	0.3

zero gradient for velocity at the outlet. At the outer walls of the fluid domain a no-slip boundary condition has been imposed. At the inner boundary of the fluid domain i.e. the fluid structure interface the fluid velocity is equated to the velocity of the structure to impose the no-slip condition. For the pressure field a zero gradient condition has been imposed at all the boundaries except at the fluid outlet where it is given an arbitrary fixed value. The FSI simulation is carried out both with and without the synthetic turbulent fluctuations using the standard U-RANS model (k-ϵ).

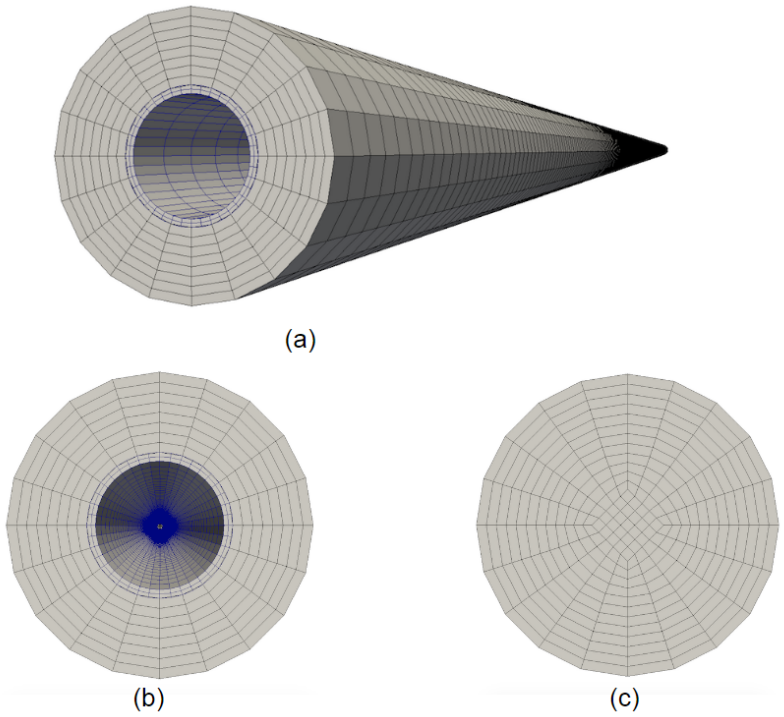

Figure 5.6: Different view of the computational mesh uses for the the fluid (black) and structure domain (blue). (a) Isometric view (b) Fluid Outlet (c) Fluid Inlet

5.2.3.1 Results and Discussions

Fig. 5.7 shows the time averaged velocity and pressure field along with the turbulent kinetic energy for a cross-section of the computational domain. As the aspect ratio of this geometry is quite high, a zoomed in version of the above figures is shown in Fig. 5.8.

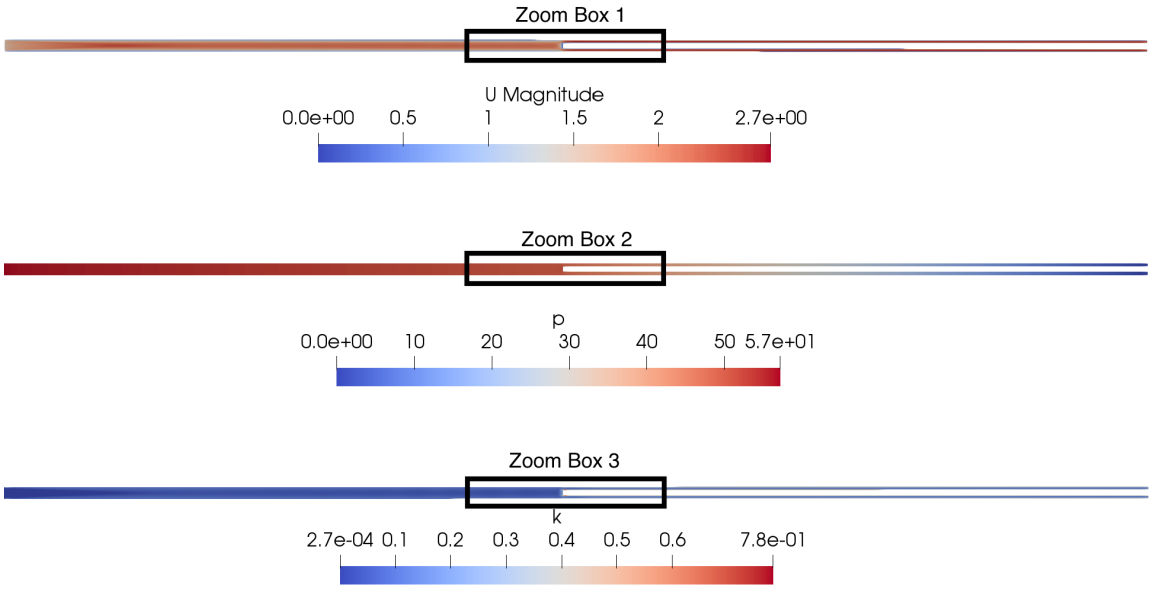

Figure 5.7: Velocity, pressure and turbulent kinetic energy field for a cross-section of the computational domain (3-D Cantilever Rod in Axial Water Flow)

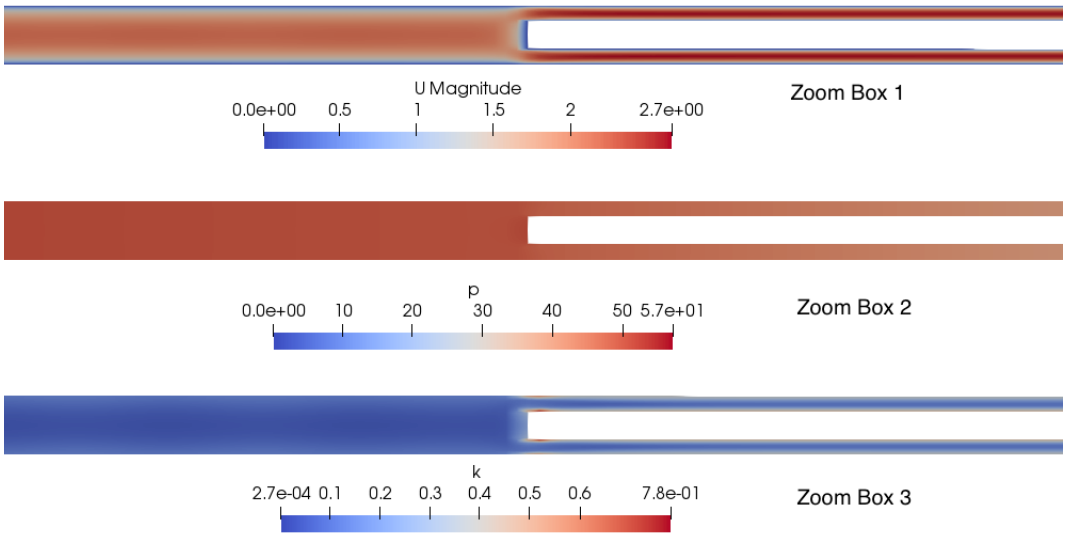

Figure 5.8: Zoomed view of the velocity, pressure and turbulent kinetic energy field for a cross-section of the computational domain (3-D Cantilever Rod in Axial Water Flow)

Fig. 5.9 and Fig. 5.10 shows the x and y component of the displacement history of a point on the rod 25 mm away from the free end of the cantilever rod both without and with the synthetic fluctuation modeling. In case of the simulation without fluctuation modeling the beam is initially displaced due to the development of the flow, but this oscillation damps out rather quickly. The order of displacement amplitudes for this case is 10^{-4} mm. In the second case the synthetic turbulent fluctuations are turned on after 0.2 second of runtime and the increase in the amplitude of oscillation can be clearly observed after that time. The displacement amplitudes for this case is 3 degrees of order higher than the one without the fluctuation modeling.

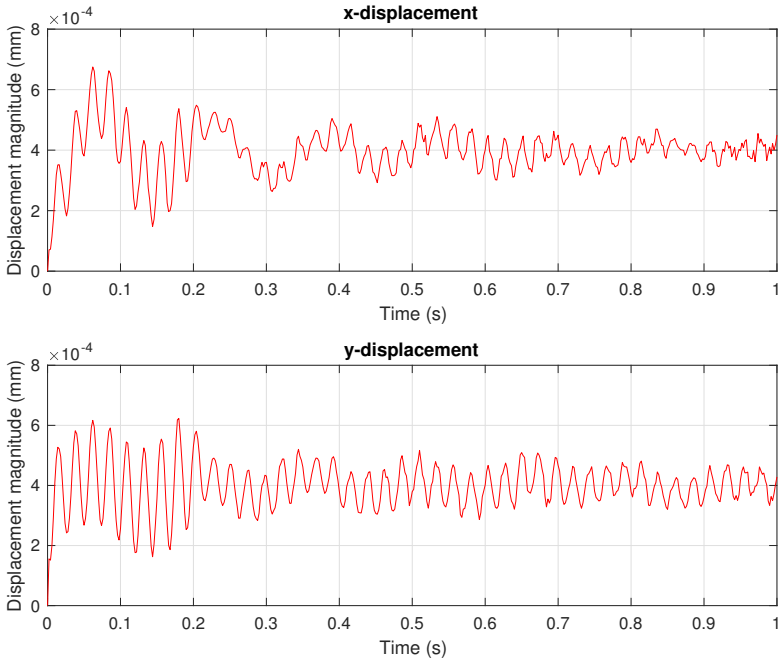

Figure 5.9: Displacement history of rod free end for U-RANS simulation without synthetic fluctuation modeling

Table 5.4: Comparison of the maximum displacement observed in the simulations with the experimental data

Maximum displacement	x- axis	y- axis	Experimental
Without Synthetic Fluctuations	6.75×10^{-4}	6.31×10^{-4}	1.80×10^{-1}
With Synthetic Fluctuations	1.45×10^{-1}	2.06×10^{-1}	

Table 5.4 compares the maximum amplitude of the cantilever rod for the FSI simulation both with and without the synthetic turbulent fluctuation modeling. Although the error in predicting the maximum amplitude of the vibrations is around 10% when compared to the experimental data, it is a significant improvement over the standard U-RANS models. A Fast Fourier Transform was also performed for the displacement signal with synthetic fluctuation modeling and the observed frequency was 5.77Hz compared to 5.68 Hz observed in the experiment.

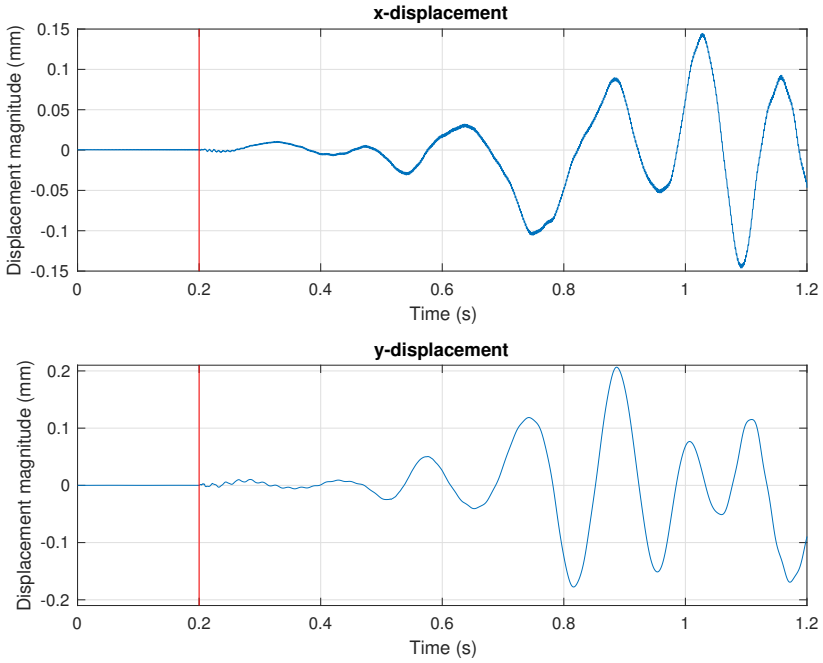

Figure 5.10: Displacement history of rod free end for U-RANS simulation with synthetic fluctuation modeling

5.3 Summary

Two test cases were performed in this chapter to verify if the synthetic turbulent fluctuation modeling can be used as an external excitation to simulate turbulence induced vibrations. The first test case consists of a 2-D steel flap hinged on both ends submerged in a turbulent water flow. It was observed that the synthetic fluctuation modeling is able to excite the steel flap indefinitely, whereas the same case with U-RANS modeling provides an initial excitement which quickly damps out. Also the magnitude of the oscillations is 2 orders of magnitude higher with the use of synthetic fluctuation modeling. To quantitatively validate this approach an experimental test case is then simulated both with and without the fluctuation modeling. The frequency of oscillation of the beam is in close agreement with the experimental data, whereas the magnitude of the oscillation shows a 10% error compared to the experiment. However the use of synthetic fluctuation modeling shows a significant improvement (3 orders of magnitude) over U-RANS simulations in the prediction of the magnitude of the vibrations.

Chapter 6

Conclusions

Within the framework of this thesis, a numerical study of the fluid structure interaction phenomenon in nuclear reactors was performed. Nuclear reactors consists of densely packed fuel rods, which are subjected to external forces due to the coolant flow around them. These forces play a critical role in the safety analysis of the structural parts of a nuclear reactor. As the densities of the coolant fluid are of the same order of magnitude as the density of the structure, the coupling between these two domains is strong. Hence, in such cases even pressure fluctuations in the flow field due to turbulence, can act as an external excitation mechanism for the fuel rods and lead to vibrations. These pressure fluctuations could be either generated locally (near-field) or due to presence of other structures upstream (far-field). This study was focused on being able to predict such Turbulence Induced Vibrations in a computationally efficient manner. One way of approaching this problem is to superimpose a synthetic turbulent fluctuation field as described earlier in Chapter 3 on top of U-RANS simulations. Hence the main research objective being,

Quantitatively verify if synthetic turbulent fluctuations modeled on top of U-RANS in a FSI solver are capable of providing a source of excitation to the structure in order to simulate Turbulence Induced Vibrations?

For this purpose an FSI solver based on coupling OpenFOAM and Deal.II using the preCICE coupling library was developed and then validated for some standard FSI benchmark test cases. The first test case used was the numerical benchmark provided by Turek and Hron (2006). This benchmark had 3 subsequent sub-cases to validate all 3 aspects of a FSI solver i.e. fluid dynamics, structural mechanics and the coupled interaction of the aforementioned. It was concluded that the simulation results were in good agreement with the reference data especially for strongly coupled problems. The second validation case was an experimental benchmark developed by Vattenfall Research and Development. In this test case initially a structure only simulation was performed to verify the replicability of the 'roller' boundary condition in structural solver. It was observed that the prediction of the oscillation frequency of the beam is dependent on the number of axial elements in the structural mesh. Also Crank-

Nicolson time marching algorithm was able to predict the amplitude of the vibrations to a greater accuracy. Using this information, a coupled FSI simulation involving the damping of an initially perturbed stainless steel beam submerged in water was performed. The damping characteristics of this beam were then studied and compared to the available experimental data. The obtained results were in good agreement with the experimental data with 0.99% error in predicting the oscillation frequency.

Finally two test cases were performed to validate the use of synthetic turbulent fluctuations as an external excitation mechanism for Turbulence Induced Vibrations. From the first test case, involving a 2-D steel flap hinged on both ends submerged in turbulent water flow, it was concluded that these pressure fluctuations are capable of providing external excitation to the structure indefinitely as long as the flow is turbulent. Another test case involving a 3-D cantilever steel beam in axial flow was then performed to quantitatively verify the aforementioned objective. It was observed from this simulation that the turbulent pressure fluctuations perform far better than the standard U-RANS approach in predicting the amplitude of the vibrations due to turbulence. Using this approach the prediction of the vibration amplitude is 3 orders of magnitude higher than standard U-RANS and shows a 10% error compared to the experimental value. The frequency of oscillation predicted with this method is nearly identical to that observed in the experiment.

Hence, it can be concluded that modeling synthetic turbulent fluctuation fields on top of the averaged velocity and pressure fields from U-RANS simulations, can be used as an external excitation mechanism for structures specifically for turbulence induced vibrations. However, even though the prediction of the vibration amplitude is considerably improved, it is still not entirely accurate. A reason for this could be certain uncertainties in the experiment. Furthermore, the synthetic fluctuation model could be further improved (e.g. introducing anisotropic turbulence) and validated against even more experimental test cases.

Appendix A

Influence of Time Marching

To study the influence of various time integration methods available in the version of the FSI solver coupled using preCICE library, a simple 1-D problem has been described in this chapter. This model problem is then further simplified to form a test case for the aforementioned analysis. Monolithic and partitioned approach (Gauss-Seidal) is used to investigate the problem. The time integration techniques investigated are backward difference 1, 2 and 3 for the fluid solver and backward difference 1, Crank-Nicolson and Newmark-beta method for the solid solver.

A.1 Model Problem

The test case is the 1-D piston problem (Piperno et al., 1995) . The geometry consists of a tube filled with gas, the left wall is fixed and the right wall is a piston of mass m. This piston is attached to a massless spring of stiffness k, with the other side of the spring being fixed to wall. The configuration has been shown in Fig.A.1.

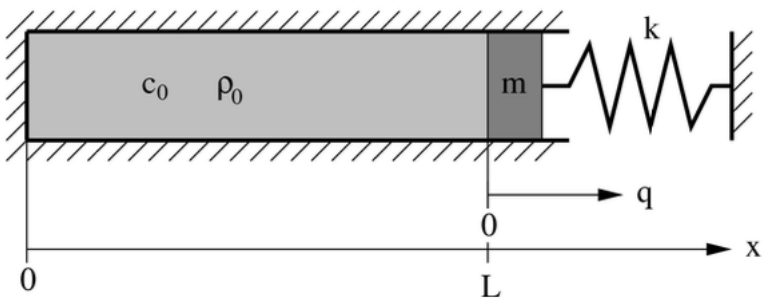

Figure A.1: 1-D piston problem

At the equilibrium position the fluid domain has length L, density ρ_0 and speed of sound c_0. The structural displacement q is defined as the displacement about this equilibrium position. Although shear stress can contribute to the energy exchange at the fluid-structure interface, it is dwarfed by the energy exchange contribution due to pressure. For this reason viscous effects are ignored and hence the Euler equations are used as the governing equations. Also gravity effects are ignored and the fluid is assumed to be an ideal gas.

A.1.1 Equations governing the fluid and structure domain

The Euler equations governing the fluid flow and the equations governing the linear structural dynamics are

$$\left.\begin{array}{l} \frac{\partial \rho}{\partial t} + \frac{\partial \rho u}{\partial x} = 0 \\ \frac{\partial \rho u}{\partial t} + \frac{\partial \rho u^2}{\partial x} + \frac{\partial p}{\partial x} = 0 \\ p = \frac{p_0}{\rho_0^\gamma}\rho^\gamma \end{array}\right\} \text{Equations governing fluid domain} \tag{A.1}$$

$$\left.m\frac{d^2q}{dt^2} + kq = (p - p_0)A\right\} \text{Equation governing structure domain} \tag{A.2}$$

The above equations can be linearized by considering small perturbations around the equilibrium state i.e. $\rho = \rho_0$, $\rho u = 0$ and $q = 0$ and then scaling the resultant equations to the equilibrium position by substituting the equations shown below into Eqs.(A.1) and (A.2),

$$\rho = \rho_0 + \rho', \;\; u = u', \;\; p = p_0 + c_0^2\rho' \;\; and \;\; q = q'$$

we get the following set of non-dimensional equations (eliminating all 2nd and higher order terms) governing the model problem.

$$\frac{\partial \overline{\rho}'}{\partial \overline{t}} + \frac{\partial \overline{\rho u}}{\partial \overline{x}} = 0 \tag{A.3}$$

$$\frac{\partial \overline{\rho u}}{\partial \overline{t}} + \frac{\partial \overline{\rho}'}{\partial \overline{x}} = 0 \tag{A.4}$$

$$\frac{d\overline{\dot{q}}'}{d\overline{t}} + \overline{\omega}^2\overline{q}' = \frac{\overline{\rho}'}{\overline{m}} \tag{A.5}$$

where $\overline{t} = \frac{c_0 t}{L}$, $\overline{x} = \frac{x}{L}$, $\overline{\rho}' = \frac{\rho'}{\rho_0}$, $\overline{\rho u'} = \frac{\rho_0 u'}{\rho_0 c_0}$, $\overline{q}' = \frac{q'}{L}$, $\overline{\omega}^2 = \frac{L^2 k}{c_0^2 m}$ and $\overline{m} = \frac{m}{\rho_0 L}$.

The fluid domain is simplified further by assuming that it doesn't deform and discretized using a cell centered Finite Volume approach. The interaction between the fluid and the solid domain is imposed by using a boundary condition that forces the velocity perturbation at the interface be equal to the piston velocity. This along with the no slip boundary condition on the left boundary of the piston are shown in Eq. (A.6).

$$u(\overline{x} = 0) = 0 \quad and \quad u(\overline{x} = 1) = \dot{q} \tag{A.6}$$

Two ghost cells can be defined at the left and the right boundary of the piston. The state vector for these cells can be obtained by using the boundary conditions and the governing fluid equations (Eq. A.6, A.3 and A.4) and are shown below, where index 0 refers to the left and N+1 refers to the right ghost cell respectively. All the state vectors used further comprise of perturbations and hence the bar over the variables has been dropped for convenience.

$$\begin{pmatrix} \rho'_{N+1} \\ \rho u'_{N+1} \end{pmatrix} = \begin{pmatrix} \rho'_N \\ -\rho u'_N \end{pmatrix} + \begin{pmatrix} -\Delta x \ddot{q}' \\ 2\dot{q}' \end{pmatrix} \tag{A.7}$$

$$\begin{pmatrix} \rho'_0 \\ \rho u'_0 \end{pmatrix} = \begin{pmatrix} \rho'_1 \\ -\rho u'_1 \end{pmatrix} \tag{A.8}$$

The pressure perturbation at the interface (p'_I) can be written as the average of that on either side of the piston, hence the density perturbation can be written as

$$\rho'_I = \frac{\rho'_N + \rho'_{N+1}}{2} \tag{A.9}$$

Using Eqs. (A.9), (A.7) and (A.5) ρ'_{N+1} can be written as

$$\rho'_{N+1} = \frac{\overline{m} - \frac{\Delta x}{2}}{\tilde{m}} \rho'_N + \frac{\Delta x}{\tilde{m}} \overline{k} q \tag{A.10}$$

where $\tilde{m} = \overline{m} + \frac{\Delta x}{2}$

Using Eqs. (A.9) and (A.10) the structural equation can be rewritten as

$$\ddot{q} + \tilde{w}^2 q = \frac{\rho'_N}{\tilde{m}} \tag{A.11}$$

Using the aforementioned equations the governing equation for each fluid cells and the piston can we written as

$$\dot{\mathbf{w}} + \begin{pmatrix} A_f & A_{fs} \\ A_{sf} & A_s \end{pmatrix} \mathbf{w} = 0 \tag{A.12}$$

with $\mathbf{w} = (\mathbf{w_f} \;\; \mathbf{w_s})^T$ with $\vec{w}_{fi} = \begin{pmatrix} \rho'_i \\ \rho u'_i \end{pmatrix}$, $\vec{w}_s = \begin{pmatrix} \dot{q} \\ q \end{pmatrix}$ A_{fi} depends on whether the fluid cell is

on the left or right boundary of the system i.e. i=1 or i=N, or it is in the interior of the fluid domain. Depending on its position A_{fi} can be written as

$$A_{f1} = \begin{pmatrix} 0 & 1 & 0 & 1 \\ -1 & 0 & 1 & 0 \end{pmatrix}, \;\; A_{fi} = \begin{pmatrix} 0 & -1 & 0 & 0 & 0 & 1 \\ -1 & 0 & 0 & 0 & 1 & 0 \end{pmatrix} \;\; A_{fN} = \begin{pmatrix} 0 & -1 & 0 & -1 \\ -1 & 0 & \frac{\overline{m} - 0.5 \cdot \Delta x}{\tilde{m}} & 0 \end{pmatrix}$$

and A_s is defined as

$$A_s = \begin{pmatrix} 0 & 1 \\ -\tilde{w}^2 & 0 \end{pmatrix}$$

The coupling matrices A_{fs} and A_{sf} are shown below:

$$A_{sf} = \begin{pmatrix} 0 & \dots & 0 & -\frac{1}{\tilde{m}} & 0 \\ 0 & \dots & 0 & 0 & 0 \end{pmatrix}$$

$$A_{fs} = \begin{pmatrix} 0 & \dots & 0 & 2 & 0 \\ 0 & \dots & 0 & 0 & \Delta x \tilde{\omega}^2 \end{pmatrix}^T$$

A.2 Time Integration

In the previous section, the semi-discrete form of the governing equation for the 1-D piston problem was derived and is shown below

$$\dot{\mathbf{w}} + \begin{pmatrix} A_f & A_{fs} \\ A_{sf} & A_s \end{pmatrix} \mathbf{w} = 0 \tag{A.13}$$

This system can either be solved simultaneously for both the fluid and the structure domain or in partitioned way. By using suitable time integration techniques this semi discrete system is first converted into a fully-discrete form. The effect of various time integration schemes is then studied by solving the fully-discrete system in a partitioned way.

A.2.1 Monolithic Approach

The above semi discrete system is solved using Backward Difference Formula-2 time integration scheme in this section. This has been shown below

$$\Big(\frac{1.5\mathbf{w}^{n+1} - 2\mathbf{w}^{n} + 0.5\mathbf{w}^{n-1}}{\Delta t}\Big) + A\mathbf{w}^{n+1} = 0 \tag{A.14}$$

where A = $\left(\begin{smallmatrix} A_f & A_{fs} \\ A_{sf} & A_s \end{smallmatrix}\right)$. The above equation can be rearranged to get the iteration matrix for time marching as shown below

$$\mathbf{w}^{n+1}\Big(\frac{1.5I}{\Delta t} + A\Big) = 2\frac{w^n}{\Delta t} - 0.5\frac{w^{n-1}}{\Delta t} \tag{A.15}$$

A.2.2 Partitioned Approach

In the partitioned approach the fluid and structure are considered as the sub-domains of the global problem. These sub domains are then solved separately and their interaction is imposed via boundary conditions of their interface. These sub-domains are usually iteratively solved a few times to satisfy the interface conditions.

Gauss-Seidal (S→F)

In this approach first structural equations are solved using the known fluid state from the previous iteration to get the new estimate for structural state ($\dot{q}$ and q). This new structural

Table A.1: Time integration methods analyzed for the fluid and structure sub-domains

Fluid-Domain	Structure-Domain
Backward Differentiation Formula - 1	Backward Differentiation Formula - 1
Backward Differentiation Formula - 2	Crank-Nicolson (CN) Method
Backward Differentiation Formula - 3	Newmark-Beta Method ($\gamma = 1/2$ and $\beta = 1/4$)

state is then transferred onto the fluid domain to get a new estimate for the fluid state variables. This process is repeated until the interface conditions are sufficiently converged. The system of equations to be solved (in order) are shown below

$$\dot{\mathbf{w}}_s + A_{sf}\mathbf{w}_f^{i-1} + A_s\mathbf{w}_s^i = 0 \tag{A.16}$$

$$\dot{\mathbf{w}}_f + A_f\mathbf{w}_f^i + A_{sf}\mathbf{w}_s^i = 0 \tag{A.17}$$

It is clear from the above equations that in structural system the term involving the interaction (A_{sf}) is solved explicitly by using the fluid state of the previous iteration, whereas in the fluid sub-domain all the terms are implicit. The error caused due to the explicit treatment of the interaction term in this case is called the partitioning error. The time integration schemes used for the fluid and the structure domain are shown in Table A.1 below

A.3 Numerical Results

The numerical analysis of the 1-D piston problem is carried out using the monolithic approach (BDF2) and all the 9 possible permutations of the time marching methods available for the fluid and structure integration (except for BDF3 for fluid sub-domain, the reason for this is explained later). The simulation parameters are $\overline{m} = 2$ and $\overline{k} = 1.429$. In this configuration the flow has a significant influence on the structural domain without completely dominating it. The piston is prescribed zero velocity ($\dot{q} = 0$) and displacement (q) equal to 1 as initial conditions. The initial density perturbation field has been prescribed using the analytical solution, with zero velocity as the initial condition. Fig. A.2 shows the velocity and displacement of the piston for five time periods of the piston oscillation.

In the following section the effect of time integration methods is studied by calculating the fluid density error and the structural velocity error after a time of 2 oscillations of the piston (i.e. t = 12.4). The errors are computed using the temporally exact solution as the reference. The mathematical modeling error is neglected in this case, hence obtaining the exact solution of the mathematical model of the proposed problem becomes the objective and is considered

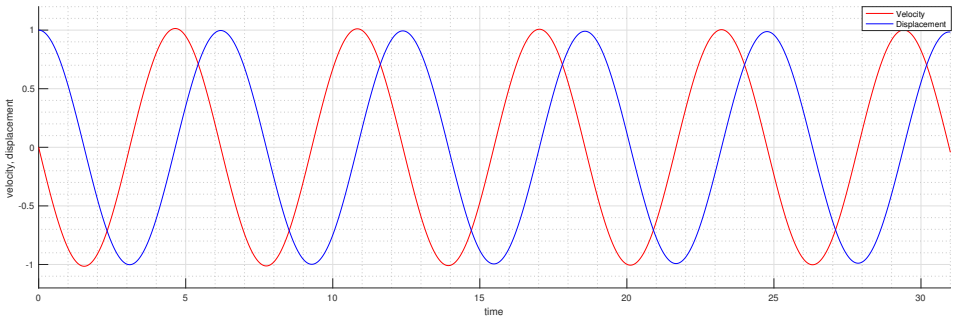

Figure A.2: Structural displacement and velocity for the 1-D piston problem

as 'exact solution'. The discretization error is the difference between the discrete solution and the exact solution as shown below

$$\epsilon_{disc}(\Delta x, \Delta t) = u_{exact} - u(\Delta x, \Delta t) \tag{A.18}$$

The discretization error itself comprises of the temporal and the spatial discretisation error,

$$\epsilon_{disc}(\Delta x, \Delta t) = [u_{exact} - \lim_{\Delta x \to 0} u(\Delta x, \Delta t)] + [u_{exact} - \lim_{\Delta t \to 0} u(\Delta x, \Delta t)] \tag{A.19}$$

Since this study is focused on time integration methods, the temporal discretization error is more relevant. However this would require infinite spatial resolution. Hence the reference solution is chosen as the temporally exact solution i.e. a solution with a very small time step (1e-4) and a fixed spatial resolution (128 fluid elements).

$$u_{ref} = u(\Delta x_0, \delta t), \qquad \Delta x_0 \text{ corresponding to 128 fluid cells} \tag{A.20}$$

Fig. A.3, Fig. A.4 and Fig. A.5 shows the root mean square of the piston velocity error, the L-2 norm of the error in density perturbation field and the root mean square of the piston displacement error respectively for different time steps varying from 0.5 to 1e-3.

It can be observed from the 3 figures above that Backward Difference Formula (BDF) 2 for fluid sub-domain with Crank-Nicolson for the structure domain has the least error. The combination of BDF1/CN for the fluid and the structural domain performs the second best, followed by BDF2/Newmark-Beta, BDF2/BE and BDF1/BE. The combination of BDF1 for the fluid domain and Newmark-Beta method for the structural domain is the least accurate.

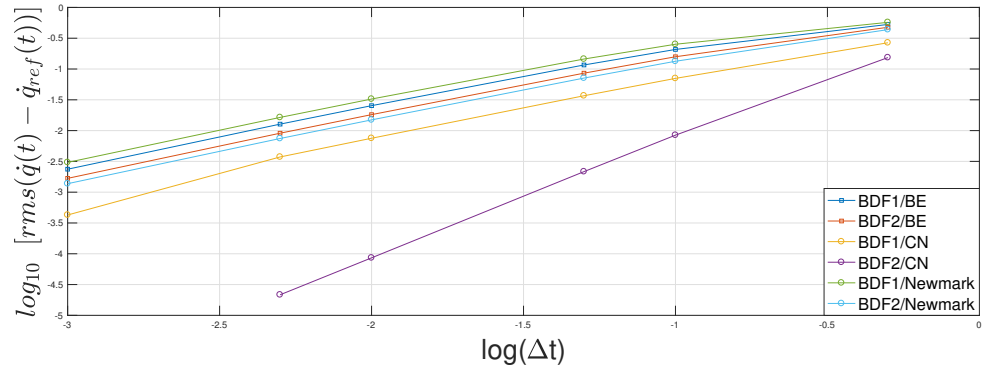

Figure A.3: Structural velocity error

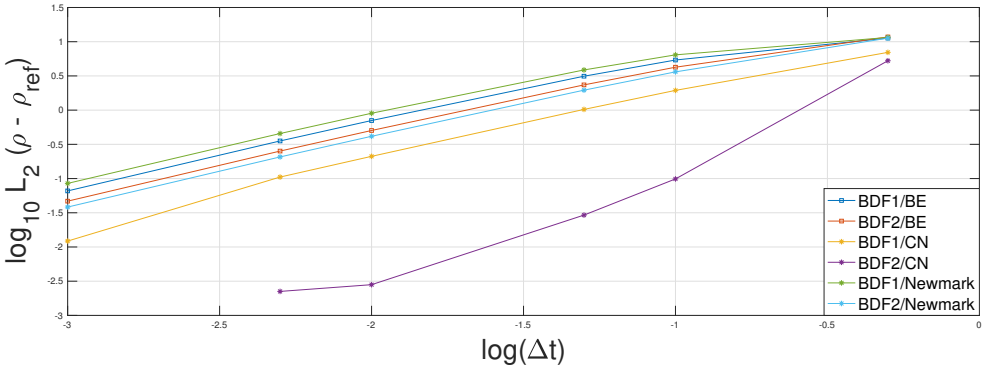

Figure A.4: Fluid density perturbation field error

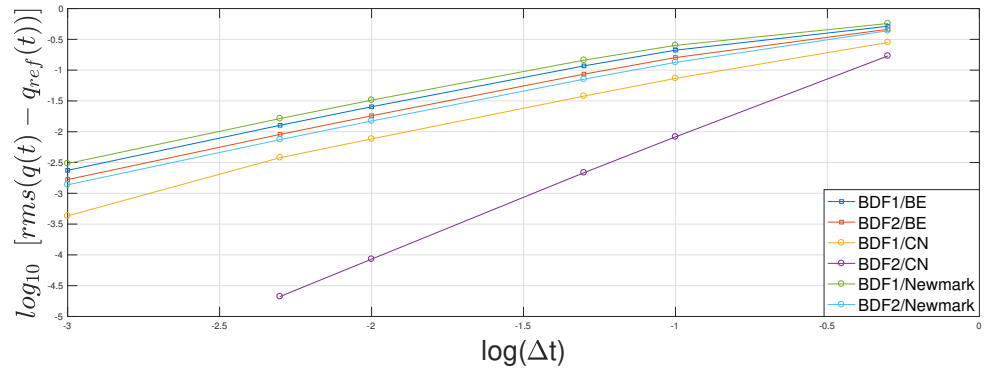

Figure A.5: Structural displacement error

It is also observed that the combination of BDF2 and CN for fluid and structure domain respectively, results in a second order accuracy, whereas all the other combinations are first order accurate.

Partitioning error can be calculated using the difference between the monolithic solution and the partitioned solution. In this case, the monolithic solution with Backward Euler approach is used as a reference (to calculate the error) for the partitioned Gauss-Seidal method using Backward Euler for both the fluid and the structure domain. Therefore the partitioning error of the time integration can be written as

$$\epsilon_{partitioning} = u_{mono}(\Delta x, \Delta t) - u_{partitioned}(\Delta x, \Delta t) \tag{A.21}$$

Fig. A.6 below shows the variation of the partitioning error (in terms of the the fluid density perturbation field error and structural velocity error) with decreasing time step sizes. It can be observed from this figure that the Gauss-Seidal partitioning approach is first order accurate. This implies that the slopes of Fig. A.3, Fig. A.4 and Fig. A.5 are not representative of the order of accuracy of the used time integration configuration alone, i.e. a drop in order of accuracy may be introduced due to the partitioning error. Hence those figures are more representative of the accuracy of the used time integration methods.

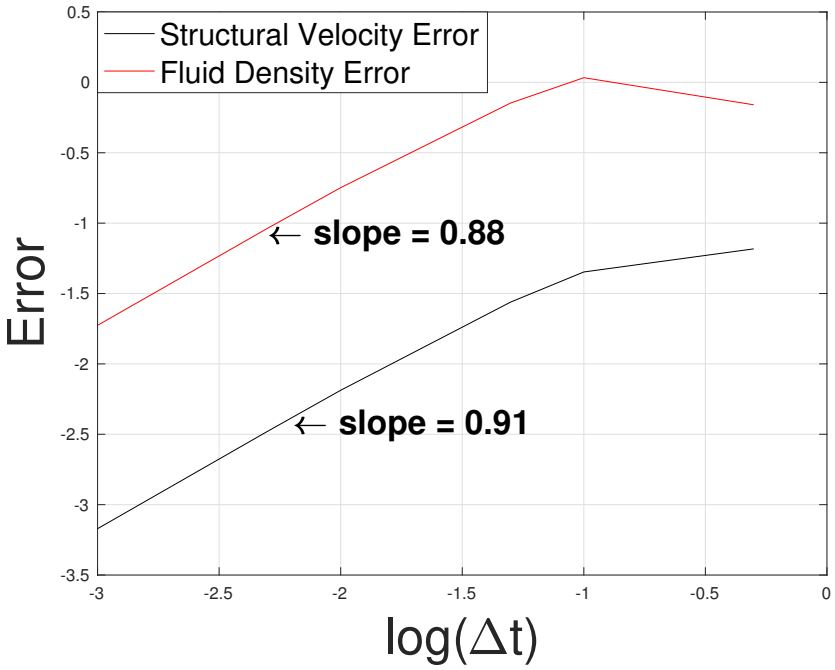

Figure A.6: Partitioning error

The results for all the possible combinations while using BDF3 have not been shown as it was observed that BDF3 was unstable upto $\Delta t = 0.001$. The reason for this has been shown for the monolithic BDF1 case. Considering Eq. (A.13), the eigenvalues of the system matrix $\mathbf{A}$ can be calculated and compared with the stability region for BDF3. The eigenvalues of the system matrix are almost aligned to the imaginary axis as $\mathrm{Re}(\lambda) \approx 0$. Fig.A.7 shows the eigenvalues for the system matrix for $\Delta t = 0.01$ and the unstable regions for BDF1, BDF2

and BDF3. Some of the eigenvalues are within the unstable region of BDF3 scheme (as can be seen in Fig. A.8 and hence the amplification factors of the corresponding errors modes are greater than 1, making the scheme unstable.

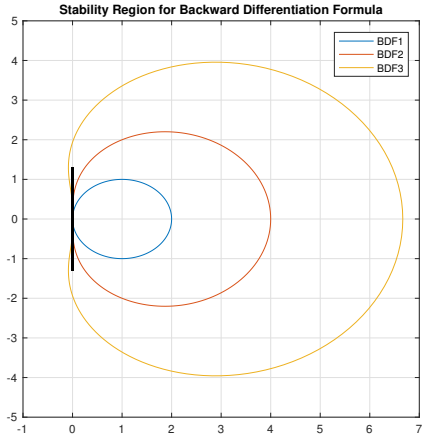

Figure A.7: Eigenvalues of matrix A corresponding to Eq. (A.13) with reference to the stability regions of BDF1, 2 and 3

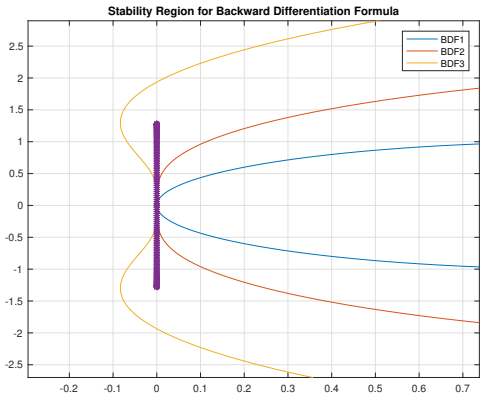

Figure A.8: Closeup of the eigenvalues (showing some are within the instability region of BDF3)

Bibliography

Bernhard Gatzhammer. *Efficient and flexible partitioned simulation of fluid-structure interactions*. Verlag Dr. Hut, 2014.

Jason Paul Sheldon. A comparison of fluid-structure interaction coupling algorithms using the finite element method. 2012.

KH Luk. Boiling-water reactor internals aging degradation study. *ORNL NUREG/CR-5754*, pages 22–24, 1993.

MP Paı et al. Real-life experiences with flow-induced vibration. *Journal of fluids and structures*, 22(6):741–755, 2006.

DS Weaver, S Ziada, MK Au-Yang, SS Chen, MP Paıdoussis, and MJ Pettigrew. Flow-induced vibrations in power and process plant componentsprogress and prospects. *Journal of Pressure Vessel Technology*, 122(3):339–348, 2000.

DS Weaver. On flow induced vibrations in hydraulic structures and their alleviation. *Canadian Journal of Civil Engineering*, 3(1):126–137, 1976.

Robert D Blevins. Flow-induced vibration. 1990.

Peter Wriggers. *Nonlinear finite element methods*. Springer Science & Business Media, 2008.

Charles Hirsch. *Numerical computation of internal and external flows: The fundamentals of computational fluid dynamics*. Butterworth-Heinemann, 2007.

Henrik Rusche. *Computational fluid dynamics of dispersed two-phase flows at high phase fractions*. PhD thesis, Imperial College London (University of London), 2003.

CM Rhie and W Li Chow. Numerical study of the turbulent flow past an airfoil with trailing edge separation. *AIAA journal*, 21(11):1525–1532, 1983.

Hrvoje Jasak. Error analysis and estimation for finite volume method with applications to fluid flow. 1996.

Suhas Patankar. *Numerical heat transfer and fluid flow*. CRC press, 1980.

Samir Muzaferija. *Adaptive finite volume method for flow prediction using unstructured meshes and multigrid approach*. PhD thesis, University of London UK, 1994.

Joris Degroote. Partitioned simulation of fluid-structure interaction. *Archives of Computational Methods in Engineering*, 20(3):185–238, 2013.

Gene H Golub and Charles F Van Loan. *Matrix computations*, volume 3. JHU Press, 2012.

Hendrik Tennekes and John Leask Lumley. *A first course in turbulence*. MIT press, 1972.

Gary I Chapman and Murray Tobak. Chapter ii. observations, theoretical ideas, and modeling of turbulent flowspast, present, and future. *Applied Mathematical Sciences Volume 58*, page 19, 1985.

Peter S Bernard and James M Wallace. *Turbulent flow: analysis, measurement, and prediction*. John Wiley & Sons, 2002.

JO Hinze. Turbulence mcgraw-hill. *New York*, 218, 1975.

Gerald Recktenwald. The k- turbulence model, 2009.

J Boussinesq. Théorie de lécoulement tourbillant. *Mem. Présentés par Divers Savants Acad. Sci. Inst. Fr*, 23(46-50):6–5, 1877.

Brian Edward Launder and Dudley Brian Spalding. The numerical computation of turbulent flows. *Computer methods in applied mechanics and engineering*, 3(2):269–289, 1974.

Jeroen De Ridder, Joris Degroote, Katrien Van Tichelen, Paul Schuurmans, and Jan Vierendeels. Modal characteristics of a flexible cylinder in turbulent axial flow from numerical simulations. *Journal of Fluids and Structures*, 43:110–123, 2013.

Shoei-sheng Chen and Martin W Wambsganss. Parallel-flow-induced vibration of fuel rods. *Nuclear Engineering and Design*, 18(2):253–278, 1972.

Robert H Kraichnan. Pressure fluctuations in turbulent flow over a flat plate. *The Journal of the Acoustical Society of America*, 28(3):378–390, 1956.

Yu Shu Chen. A root-mean-square pressure fluctuations model for internal flow applications. 1985.

S. Senthooran. *A Computational Model to Calculate Flow-Induced Pressure Fluctuations on a Bluff Body*. PhD thesis, Texas Tech University, 2002.

Lewis Fry Richardson. *Weather prediction by numerical process*. Cambridge University Press, 2007.

Andrey Nikolaevich Kolmogorov. Energy dissipation in locally isotropic turbulence. In *Dokl. Akad. Nauk. SSSR*, volume 32, pages 19–21, 1941.

Mattias Billson. *Computational techniques for turbulence generated noise*. Chalmers University of Technology, 2004.

OpenFOAM. *User Guide, Version 2.2.0*. OpenFOAM Foundation, 2013 .

W. Bangerth, D. Davydov, T. Heister, L. Heltai, G. Kanschat, M. Kronbichler, M. Maier, B. Turcksin, and D. Wells. The `deal.II` library, version 8.4. *Journal of Numerical Mathematics*, 24, 2016.

Hans-Joachim Bungartz, Florian Lindner, Bernhard Gatzhammer, Miriam Mehl, Klaudius Scheufele, Alexander Shukaev, and Benjamin Uekermann. precice – a fully parallel library for multi-physics surface coupling. *Computers and Fluids*, 141:250—-258, 2016.

Serge Piperno, Charbel Farhat, and Bernard Larrouturou. Partitioned procedures for the transient solution of coupled aroelastic problems part i: Model problem, theory and two-dimensional application. *Computer methods in applied mechanics and engineering*, 124 (1-2):79–112, 1995.

S. Kottapalli. Numerical prediction of flow induced vibrations in nuclear reactors through pressure fluctuation modelling. 2016.

Stefan Turek and Jaroslav Hron. Proposal for numerical benchmarking of fluid-structure interaction between an elastic object and laminar incompressible flow. In *Fluid-structure interaction*, pages 371–385. 2006.

Angele K. Lundqvist G. Edh N. Lillberg, E. Tailored experiments for validation of cfd with fsi for nuclear applications. 2015.

Eline Ter Hofstede. Numerical study of fluid structure interaction in nuclear reactor applications. 2015.

Sundaramoorthy Rajasekaran. *Structural dynamics of earthquake engineering: theory and application using MATHEMATICA and MATLAB*. Elsevier, 2009.

Chunyuan Liu, Andrea Cioncolini, Jorge Silva Leon, Dennis Cooper, and Hector Iacovides. Experimental study of a flexible cantilever rod subjected to axial water flow.